THE SPECTRAL AND TEMPORAL PROPERTIES OF MAXI J1409-619

A THESIS SUBMITTED TO
THE GRADUATE SCHOOL OF NATURAL AND APPLIED SCIENCES
OF
MIDDLE EAST TECHNICAL UNIVERSITY

BY

ÇAĞATAY KEREM DÖNMEZ

IN PARTIAL FULFILLMENT OF THE REQUIREMENTS
FOR
THE DEGREE OF MASTER OF SCIENCE
IN
PHYSICS

FEBRUARY 2019

Approval of the thesis:

THE SPECTRAL AND TEMPORAL PROPERTIES OF MAXI J1409-619

submitted by **ÇAĞATAY KEREM DÖNMEZ** in partial fulfillment of the requirements for the degree of **Master of Science in Physics Department, Middle East Technical University** by,

Prof. Dr. Halil Kalıpçılar
Dean, Graduate School of **Natural and Applied Sciences** _____

Prof. Dr. Altuğ Özpineci
Head of Department, **Physics** _____

Prof. Dr. Altan Baykal
Supervisor, **Physics, METU** _____

Examining Committee Members:

Prof. Dr. Sıtkı Çağdaş İnam
Electrical and Electronics Engineering, Başkent University _____

Prof. Dr. Altan Baykal
Physics, METU _____

Assoc. Prof. Dr. Sinan Kaan Yerli
Physics, METU _____

Date:

I hereby declare that all information in this document has been obtained and presented in accordance with academic rules and ethical conduct. I also declare that, as required by these rules and conduct, I have fully cited and referenced all material and results that are not original to this work.

Name, Surname: Çağatay Kerem Dönmez

Signature :

ABSTRACT

THE SPECTRAL AND TEMPORAL PROPERTIES OF MAXI J1409-619

Dönmez, Çağatay Kerem
M.S., Department of Physics
Supervisor: Prof. Dr. Altan Baykal

February 2019, 67 pages

In this thesis, spectral and timing analysis of the transient high-mass X-ray binary (HMXB) pulsar MAXI J1409-619 are presented. MAXI J1409-619 was discovered in October 2010, and went into an outburst in early December 2010 until February 2011. Observations of *Swift* and *RXTE* throughout this period are used in the thesis.

The analysis results are in line with the assertion that MAXI J1409-619 is an accretion-powered pulsar. Time-resolved energy spectra of RXTE and Swift data confirm the previously reported findings. At the peak outburst, the spectra are modeled with a power law with a high energy cutoff, plus a Gaussian Fe line fixed at 6.4 keV. On the other hand, a simple power law model is used in observations with unsufficiently low count rates. Absorption-corrected peak flux on MJD 55534 is calculated to be 1.96×10^{-9} erg s^{-1} cm^{-2} in 3–25 keV range. Assuming a distance of $\sim$14.5 kpc, corresponding peak luminosity is $L_{3\text{-}25keV} \sim 4.9\times10^{37}$ erg s^{-1}. Furthermore, evolution of spectral parameters of the source and the correlations between these parameters are studied.

Throughout the outburst stage, periodic variability in the light curves becomes evident.

$P_{spin} \sim 503$ s is found at the outburst onset. Using phase-resolved spectroscopy, a double-peaked pulse profile is verified, and spectral parameters with changing phases are investigated.

Lastly, power spectral analysis confirms the existence of quasi-periodic oscillations (QPO) and their harmonics in MAXI J1409-619. As the outburst progresses, centroid frequency of the QPOs shifts from $\sim$0.2 Hz to $\sim$0.1 Hz, implying the QPO features are linked with flux and mass transfer rates. Two observations on MJD 55541 with 19 ks exposure reveals a QPO at 0.190 Hz with two harmonics, implying a magnetic field of $\sim 1 \times 10^{13}$ G.

Keywords: neutron stars, X-ray binaries, accretion-powered pulsars, quasi-periodic oscillations, MAXI J1409-619

ÖZ

MAXI J1409-619'UN TAYFSAL VE ZAMANSAL ÖZELLİKLERİ

Dönmez, Çağatay Kerem
Yüksek Lisans, Fizik Bölümü
Tez Yöneticisi: Prof. Dr. Altan Baykal

Şubat 2019 , 67 sayfa

Bu tezde, süreksiz yüksek kütleli X-ışını çift yıldız sistemi atarcası MAXI J1409-619'un tayfsal ve zamansal analizleri sunulmaktadır. Ekim 2010'da keşfedilen MAXI J1409-619, Aralık 2010'da, Şubat 2011'e kadar sönümlenen bir patlama geçirmiştir. Tezde *Swift* ve *RXTE* uydularının bu süre zarfındaki gözlemleri kullanılmıştır.

Analiz sonuçları MAXI J1409-619'un bir aktarım güçlü atarca olduğu savıyla uyumludur. RXTE ve Swift verisinin zamana göre çözümlenmiş enerji tayfları önceden raporlanan bulguları doğrulamaktadır. Patlamanın doruğunda, tayflar yüksek enerji kesimli (*cutoff*) güç yasası (*power law*) ve 6.4 keV'ta sabitlenmiş bir Fe çizgisi ile modellenmiştir. Öte yandan, yetersiz derecede düşük sayım oranı içeren gözlemlerde basit güç yasası kullanılmıştır. Soğurulma düzeltmesinin yapıldığı 3–25 keV aralığındaki en yüksek akı, 1.96×10^{-9} erg s^{-1} cm^{-2} olarak hesaplanmıştır. 14.5 kiloparseklik bir uzaklık varsayıldığında buna karşılık gelen aydınlatma gücü $L_{3\text{-}25keV} \sim 4.9\times10^{37}$ erg s^{-1} dir. Ayrıca, kaynağın tayfsal değişkenlerinin evrimi ve bu değişkenler arasındaki bağıntılar üzerinde çalışılmıştır.

Patlama evresi boyunca ışık eğrisinde periyodik değişkenlikler ortaya çıkmıştır. Pat-

lama başlangıcında 503 saniyelik bir dönüş periyodu bulunmuştur. Çeşitli yörünge evrelerinde yapılan tayf ölçümleri kullanılarak çift tepeli atım profilinin varlığı doğrulanmış, değişen yörünge fazlarındaki tayfsal değişkenler incelenmiştir.

Son olarak, güç tayfı analizleri MAXI J1409-619'da periyodik benzeri salınımlar (QPO) ve harmoniklerinin varlığını doğrulamıştır. Patlama süresince periyodik benzeri salınımların frekansları $\sim$0.2 Hz'den $\sim$0.1 Hz'e doğru kaymıştır, bu da periyodik benzeri salınımların akı ve kütle aktarım hızıyla bağlantılı olduğuna işaret etmektedir. MJD 55441'deki toplamda 19 ks pozlamalı iki gözlem, 0.190 Hz'de bir periyodik benzeri salınım ve iki harmoniğini ortaya çıkarmıştır; bu da $\sim 1 \times 10^{13}$ Gauss kuvvetinde bir manyetik alanı işaret etmektedir.

Anahtar Kelimeler: nötron yıldızları, X-ışını çiftleri, aktarım güçlü atarcalar, periyodik benzeri salınımlar, MAXI J1409-619

to my family and friends

ACKNOWLEDGMENTS

I would like to express my sincere gratitudes to my supervisor Prof. Dr. Altan Baykal for giving me the opportunity of working with him. I am very grateful for his guidance and encouragement during my studies. I also thank Prof. Dr. Sıtkı Çağdaş İnam and Assoc. Prof. Dr. Sinan Kaan Yerli for their invaluable comments and advices.

I am indebted to my colleagues Dr. Şeyda Şahiner and Dr. Muhammed Miraç Serim for all the help and guidance they provided. Without their support, my thesis stage would be much harder. I would also like to thank our departmental secretary Gülşen Özdemir Parlak for effectively handling all sorts of bureaucratic nightmares I had fallen into throughout my master education.

Besides academical help, emotional support was also crucial throughout my thesis studies. I thank all my close friends in METU for being a part of my life, and make this stressful process more bearable. Though there are too many to name here individually, I am sure they know how important they are for me. Nevertheless, I would like to express my deep gratitudes to my old friends Yeşim İpekçi, Süleyman Bölükbaş, Cansu Aydın and Nimet Bulut for their everlasting friendships regardless of distance.

Moreover, I thank TÜBİTAK for financial support during my education through 2228 scholarship program for master students.

Finally, and most importantly, I owe my family the most. They have always stood behind me, and supported me unconditionally whenever I needed help. It is impossible to thank them adequately.

TABLE OF CONTENTS

LIST OF TABLES

TABLES

LIST OF FIGURES

FIGURES

LIST OF ABBREVIATIONS

ARF	ancillary response file
ASCA	Advanced Satellite for Cosmology and Astrophysics
ASM	All Sky Monitor
ATel	Astronomer's Telegram
BAT	Burst Alert Telescope
BeXB	Be/X-ray binary
CCD	charge coupled device
Dec.	declination
FoV	field of view
FWHM	full width at half maximum
GBM	Gamma-ray Burst Monitor
GRB	gamma-ray bursts
GSC	Gas Slit Camera
GPS	Global Positioning System
HEXTE	The High Energy X-ray Timing Experiment
HMXB	high mass X-ray binary
IM	Imaging mode
ISS	International Space Station
JAXA	Japan Aerospace Exploration Agency
LHPRS	Loop Heat Pipe and Radiation System
LMXB	low-mass X-ray binary
MJD	modified Julian date
MAXI	The Monitor of All-sky X-ray Image
NASA	National Aeronautics and Space Administration

ObsID	Observation ID
PC	Photon counting mode
PCA	Proportional Counter Array
PCU	proportional counter unit
PD	Photodiode mode
PHA	pulse height amplitude
PI	Principal Investigator
QPO	quasi-periodic oscillation
RA	right ascension
RMF	redistribution matrix file
RXTE	Rossi X-Ray Timing Explorer
SAA	South Atlantic Anomaly
SGXB	supergiant X-ray binary
SSC	Solid-state Slit Camera
ToO	target of opportunity
UVOT	Ultraviolet/Optical Telescope
VSC	Visual Star Camera
WT	Window timing mode
XRT	The X-Ray Telescope

CHAPTER 1

INTRODUCTION

1.1 General Introduction to Neutron Stars

Neutron stars are at the final stage of the evolutionary track of massive stars. A star spends its lifetime by incessantly maintaining its hydrostatic equilibrium: Fusion power created at the core of the star overcomes the tremendous force of the gravity of its mass. Small stars can stay at this phase for billions of years, using mainly hydrogen as fuel. On the other hand, massive stars consume their fuel much more rapidly and are able to "ignite" heavier elements up to iron. When a sufficiently massive star cannot sustain fusion at its core anymore, it explodes in a spectacular supernova, violently expelling its outer layers. Without any outward force to halt the immense gravitation of its mass, the core of the star squeezes incomprehensibly: It collapses into a neutron star for the stars weighing from 8 to 25 Solar masses, whereas the cores of the most massive stars collapses indefinitely to form a black hole. The core of the star is so immensely squeezed by gravitation that a neutron star has only $\sim$1/100 000th of radius of the Sun (r$\sim$10 km), yet its mass is still comparable to the Solar mass. After such a violent fate, one might consider neutron stars as dead stars, but a neutron star is far from simply being a star corpse—many of them haunt the Universe by their weird and energetic emissions. Thankfully, since their proposal of existence in 1934 by Baade and Zwicky [3], the astronomers have uncovered many of the mysteries behind these stellar remnants, yet the more it is explored, the more questions arise.

Most neutron stars are notable radio and X-ray emitters. As the Earth's atmosphere effectively blocks the X-ray spectra from the outer space, astronomers were not able

to investigate the universe in X-rays until the advent of rocketry and satellite technologies. Therefore, X-ray astronomy is a relatively new area. First detection of an extrasolar X-ray source was the discovery of Sco X-1 in 1962 [4], which is later turned out to be an accretion-powered low mass X-ray binary. The proposed model to explain the X-ray emission of Sco X-1 in 1967 laid the foundations of the theory of accreting neutron stars [5]. Furthermore, the first pulsar was discovered in radio frequencies in the same year. Though the periodic pulses were speculated to be of artificial origin, such as signals from an extraterrestrial civilization, shortly after these were shown to be indeed produced by natural mechanisms [6, 7]. This was the beginning of rotational-powered neutron star discoveries, many other pulsars were discovered in 1970s and later. Since then, the fairly new realm of the neutron stars are explored thoroughly in all wavelengths. Many instruments and space telescopes, dedicated to or capable of X-ray observations stimulated our understanding of neutron stars, such as Uhuru, Ariel 5, SAS-3, HEAO-1, Einstein, EXOSAT, Ginga, ROSAT, RXTE, BeppoSAX, Chandra, XMM-Newton, INTEGRAL, Swift, Suzaku, AGILE, MAXI, NuSTAR and NICER.

A pulsar is a type of neutron star with a powerful magnetic field. Magnetic poles of a pulsar are not aligned with the rotational axis, therefore the beam of emission continuously sweeps around the sky while the neutron star is rotating. If the beam crosses with the Earth, the pulsar appears to be making periodic pulses (see Figure

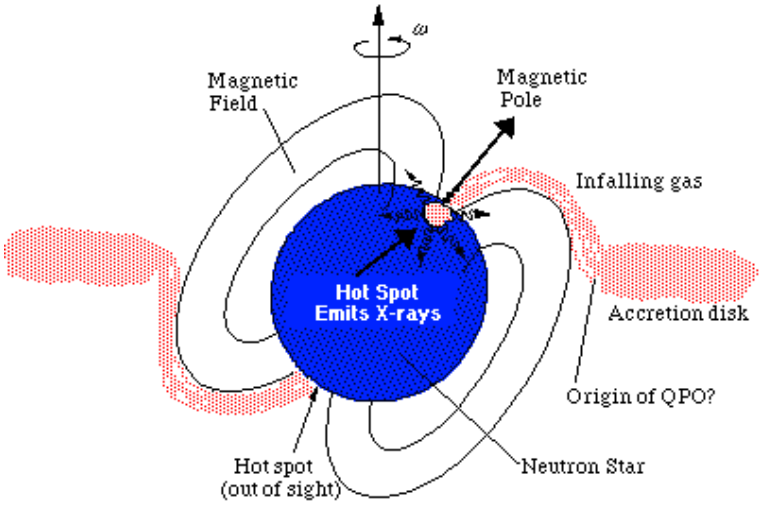

Figure 1.1: Diagram of a pulsar

1.1).

As in the case with the other compact objects, pulsars are found rather as isolated objects or in binaries. The observed isolated pulsars are powered by the rotational kinetic energy loss of the pulsar via magnetic braking. In a binary system, the main source of the energy is the mass transfer from the companion star to the pulsar. Because of the deep gravitational well the neutron star created, falling matter onto the neutron star gains tremendous amounts of kinetic energy, comparable to the nuclear energy created by the same amount of matter. The falling matter accretes rather onto an accretion disk due to its angular momentum, or directly funneled onto the magnetic poles of the pulsar by intense magnetic fields. For both cases, the conversion of the gravitational potential energy by accretion is the origin of the X-ray pulsar emission [8]. Consequently, pulsars are classified as rotational-powered and accretion-powered, depending on their sources of energy. The accretion luminosity of a pulsar can be calculated using this formula,

$$L_{acc} \approx \frac{GM\dot{M}}{R} \tag{1.1}$$

where G is the gravitational constant, M is the pulsar mass, $\dot{M}$ is the mass accretion rate of the pulsar, and R is the pulsar radius. When the source is observed from the Earth, only a miniscule amount of flux F can be detected. With a known distance d, the luminosity of the pulsar can be determined from the simple relation [9]

$$L = 4\pi d^2 F. \tag{1.2}$$

1.2 X-ray Binaries

X-ray binaries are powered by accretion, as explained in Section 1.1. The binary companion of the pulsar is also named as "donor" star, as it supplies the matter flow to the pulsar. The matter flow takes place by Roche lobe overflow or stellar wind, depending on the properties of the binary system and the companion star. Accreting X-ray pulsars have a spin period ranging from 2 ms to 10^4 seconds [7]. They also

have a very strong magnetic field, at the order of 10^{12} Gauss. The flow of matter is interrupted by this magnetic field at some point, and funneled into the magnetic poles of the pulsars as "accretion funnels". At the locations where the matter impacts at the polar regions, "hot spots" are produced. The kinetic energy of the matter is converted mainly into X-rays at these regions. The radius of the magnetospheric region where the magnetic field is dominant is defined as the *Alfvén radius*. It can be calculated as

$$r_{Alfvén} = 2.6 \times 10^8 \left[\frac{{\mu_{30}}^4 (M_{star}/M_\odot)}{{L_{37}}^2 {R_6}^2} \right]^{1/7} cm \tag{1.3}$$

where μ_{30} is the magnetic moment in units of 10^{30} G cm^3, L_{37} is the accretion luminosity in units of 10^{37} erg s^{-1} and R_6 is the radius of the pulsar in units of 10^6 cm [8]. If the magnetic field is very weak ($r_{Alfvén} < r_{pulsar}$), the accreted matter directly falls onto the pulsar surface without forming an accretion funnel.

X-ray binaries are mainly classified by the mass of the companion star, namely low-mass X-ray binaries (LMXB) and high-mass X-ray binaries (HMXB).

1.2.1 HMXBs

In HMXBs, the binary companion is an O or B type star, with a mass larger than the accreting neutron star. They emit intense X-ray radiation, at outbursts they can be the brightest objects in the sky in X-rays. There are two main types of HMXBs: Supergiant X-ray binaries (SGXB) and Be/X-ray binaries (BeXB).

1.2.1.1 SGXBs

SGXBs have a massive supergiant companion with a mass of $\sim$15–30 M$_\odot$ and of I–II luminosity class. They are powered either by a Roche lobe overflow or a dense stellar wind [10]. The systems with Roche lobe overflow should have small orbits, and high accretion rates. Therefore the orbital periods are short (P$_{orb} < 4$ days) and they have very high luminosities (L$_{X\text{-}ray} \sim 10^{37}$ erg s^{-1}), also the compact star has a rapid spin (P$_{spin} < 10$ s) because of the angular momentum gained by accretion. The systems with dense stellar systems have greater orbital periods (P$_{orb} > 4$ days)

and moderate luminosities ($L_{X\text{-}ray} \sim 10^{34}$–$10^{35}$ erg s^{-1}). It is also possible that both processes simultaneously power some SGXB systems [10]. As SGXBs are bright and persistent in X-rays, they are the first discovered subgroup among HMXBs, though it is now thought that BeXBs overpopulate SGXBs [11].

1.2.1.2 BeXBs

BeXBs have a Be type companion with IV–V luminosity class. A Be star is a non-supergiant B type star showing some distinct features, such as emission lines in its spectrum and an "infrared excess". Be stars are rapidly rotating and have a surrounding equatorial disk, but they reside entirely within their Roche lobe. The equatorial disk consisting of ionized gas is the source of the emission lines and the observed excess infrared radiation compared to the typical B type stars. This emission line property enables to distinguish them from common B type stars, thus these stars are represented with an additional qualifier "*e*" for distinction as Be stars [11].

Most BeXBs have transient nature, but persistent BeXBs also exist. Persistent BeXBs are characterized by lower luminosities ($L_{X\text{-}ray} \sim 10^{34}$–$10^{35}$ erg s^{-1}), less X-ray variability. During the outburst stage, the flux levels do not increase more than one order of magnitude. They generally host a pulsar with a low spin rate ($P_{spin} \geq 200$ s). Their spectrum also exhibits a very weak iron line at 6.4 keV (it is absent in several cases), which implies that the surroundings of the pulsar is not dense with material [11].

Transient BeXBs have two types of outbursts. Type I outbursts are periodic, occurring for short durations at the periastron passage of the neutron star. During the outbursts, the X-ray flux increases around one order of magnitude, to $L_{X\text{-}ray} \leq 10^{37}$ erg s^{-1}.

Type II outbursts are irregular, they occur independently of the orbital phase and longer in duration—they might cover multiple orbit periods. The outbursts are much more intense than Type I outbursts. The X-ray flux of a type II outburst is three–four orders of magnitude higher than the flux at the low-state. At the peak, the flux level may even reach the *Eddington luminosity*, temporarily becoming one of the brightest objects in X-ray sky. Eddington luminosity puts an upper limit to the luminosity of

the neutron star. Beyond this critical limit, the gravitational pressure cannot balance the radiation pressure and the falling matter is driven out, interrupting the energy source of the outburst. Assuming only Thompson scattering as an acting mechanism, Eddington luminosity is calculated as

$$L_{Edd} = 1.3 \times 10^{38} (M_{star}/M_{\odot})\ erg\ s^{-1} \tag{1.4}$$

where $M_{\odot}$ is the Solar mass [12]. The underlying cause of such an energetic outburst is thought to be the formation of a temporary accretion disk around the neutron star. Also, quasi-periodic oscillations are observed in some systems, which supports the idea of transient disk formation.

When the known P_{orb} and P_{spin} values of accreting X-ray binaries are plotted, which is also known as a Corbet diagram, the set of distinct subclasses of X-ray binaries are clustered in different locations and show different correlations [13] (see Figure 1.3). In this diagram, a positive correlation between P_{orb} and P_{spin} of BeXBs is clearly seen. It is thought that spin period of the BeXB pulsars eventually reach their equilibrium period, P_{eq}, which is dependent on the mass accretion rate. BeXB systems with longer orbital periods, hence with wider orbits, apparently have lower accretion rates, which correspond to longer spin periods [14].

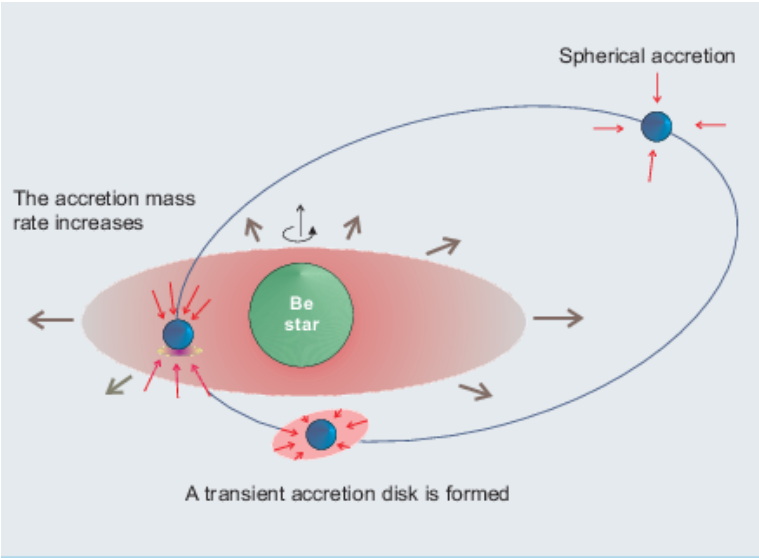

Figure 1.2: Diagram of a BeXB system [1]

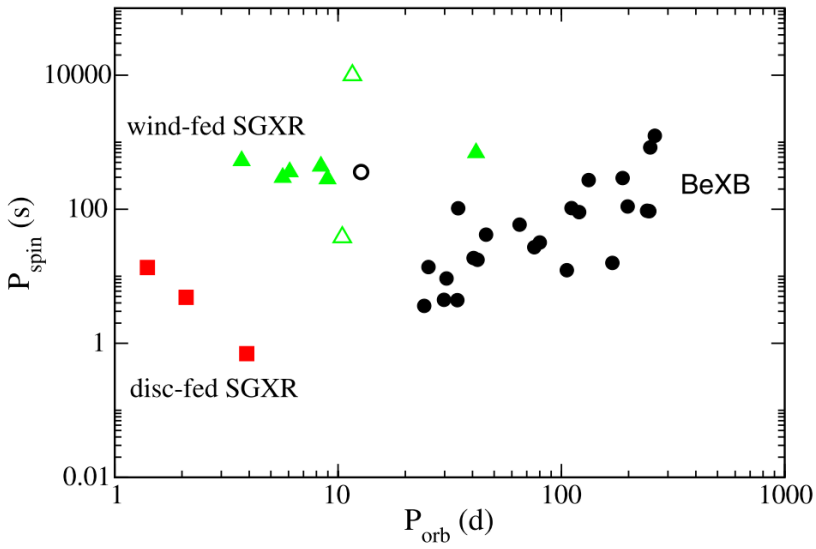

Figure 1.3: The Corbet diagram. The positive correlation between P_{orb} and P_{spin} in BeXBs can be seen.

Practically all BeXBs have a neutron star as a compact object, but at least one Be star–black hole binary is shown to exist [15].

1.3 Quasi-Periodic Oscillations (QPOs)

Many X-ray sources exhibit irregular fluctuations, flickering and pulsations in their light curves. Therefore, X-ray variability is an important property to establish a better understanding about the nature of the source. The behavior of these X-ray variabilities (whether it is transient, periodic or quasi-periodic etc.) can be better visualized by in frequency domain. Aperiodic behavior of a source can be investigated by creating a Fourier power spectrum from its light curve. To put it simply, Fourier analysis takes a signal in time domain and transforms it into frequency domain, or vice versa. Therefore, the light curve can be decomposed into many frequency components and the power of each frequency component indicates the strength of modulations at the particular frequency. If a sufficiently long light curve is given as an input (and if pulsations have enough signal-to-noise ratios), the spin period of the pulsar is seen as a very narrow spike in a power spectrum. On the contrary, slightly periodic features appear as broader peaks in a power spectrum, meaning that the periodicity is not

restricted to a constant frequency. These excess peaks are classified by the relative broadness of the features, namely, their quality factor ("Q-factor", or "Q" in short). It is defined as

$$Q = \frac{\nu_{peak}}{\Delta\nu_{peak}} \tag{1.5}$$

where ν_{peak} is the centroid frequency of the peak and $\Delta\nu_{peak}$ is the full width at half maximum (FWHM) of the peak excess. If Q<2, the excess component is considered as a "noise", and if Q>2, the peak is sufficiently narrow to be defined as a "quasi-periodic oscillation" (QPO) [11]. Ideally, QPOs appear as Lorentzian or Gaussian features over the power spectrum continuum.

QPO characteristics of HMXB and LMXB systems differ considerably. Power spectra of HMXB pulsars exhibit QPOs in 1-200 mHz range, whereas the frequency range of LMXB and black hole binary QPOs is 1-1000 Hz [11]. QPOs in LMXB systems are first detected in GX 5-1 in 1985 [16]; and later in 1989, QPOs in HMXBs are first detected in EXO 2030+375 [17]. The exact mechanism behind the origin of the QPOs is still poorly understood. Nevertheless, QPOs are thought to be originated by inhomogeneous matter flow at the inner region of the accretion disk [18]. There are two main competing models to explain the QPOs in HMXB systems.

The first one is Keplerian frequency model [19]. In that model, clumps of matter at the inner edge of the accretion disk obscure some of the outgoing flux until they disappear after revolving several cycles around the pulsar. Hence, the QPO frequency corresponds to the Keplerian frequency at the inner edge of the accretion disk ($\nu_{QPO} = \nu_K$) [20]. Keplerian frequency ν_K at the inner edge of the disk is defined as

$$\nu_K = \frac{1}{2\pi}\left(\frac{GM}{r_0^3}\right)^{\frac{1}{2}} \tag{1.6}$$

where G is the gravitational constant, M is the pulsar mass, and r_0 is the radius of the inner disk, which is defined here as

$$r_0 \approx 0.52 r_A = 0.52\mu^{\frac{4}{7}}(2GM)^{-\frac{1}{7}}\dot{M}^{-\frac{2}{7}} \tag{1.7}$$

where r_A is the Alfvén radius, $\dot{M}$ is the mass accretion rate of the pulsar, μ is the magnetic dipole moment, defined as

$$\mu = B \times R^3, \tag{1.8}$$

and R is the pulsar radius [21].

In the second model, which is referred as the beat frequency model ([22], [23]), clumps of matter at the inner edge of the accretion disk interact with the magnetosphere of the pulsar. The magnetosphere, rotating at the same rate with the pulsar, slowly removes the clump as a result of interaction and this process modifies the accretion rate. Therefore, the QPO frequency is the difference between the Keplerian frequency of the clumps at the magnetospheric boundary, and the spin frequency of the pulsar, namely the "beat frequency" ($\nu_{QPO} = \nu_K - \nu_{spin}$) [20]. As magnetospheric radius depends on mass accretion rate, ultimately QPO frequencies are linked to the mass accretion rate and the luminosity of the source.

As of 2013, 12 transient HMXB pulsars are shown to possess QPO features [18].

CHAPTER 2

INSTRUMENTS

As the atmosphere of Earth blocks X-rays from the outer space, X-ray astronomy instruments should be sent beyond the atmosphere, by high altitude balloons, rockets or satellites. Three instruments in Earth's orbit are in the scope of this thesis: Neil Gehrels Swift Observatory, Rossi X-Ray Timing Explorer (RXTE) and The Monitor of All-sky X-ray Image (MAXI).

2.1 Neil Gehrels Swift Observatory

Neil Gehrels Swift Observatory (*Swift*, previously *"Swift Gamma Ray Burst Mission"*) is a multi-wavelength space observatory. As a part of the NASA's Medium-class Explorer program (MIDEX), Swift was launched into low-Earth orbit on 20 November 2004. Mainly for observing gamma-ray bursts (GRB) and their afterglows, Swift has the capability of observing in gamma-ray, X-ray, ultraviolet and optical wavelengths. Its three co-aligned scientific instruments on-board work together to detect, locate and observe gamma-ray bursts (Figure 2.1): Burst Alert Telescope (BAT) is a gamma-ray instrument with a large FoV for GRB detection, working in 15–150 keV energy range. It detects GRBs and locates them up to 1 arc minute sensitivity, then instructs the spacecraft to slew towards the source. The X-Ray Telescope (XRT) has the capability of imaging and spectroscopy in 0.2–10 keV range, and also pinpointing GRBs with $\sim$3–5 arcseconds precision. Lastly, Ultraviolet/Optical Telescope (UVOT) is a 30 cm telescope to observe GRB afterglows, pinpoint GRBs up to 0.5 arcseconds, and create finding charts. With this configuration, within $\sim$15 seconds after detection of a GRB by BAT, the preliminary burst position can be transmitted; and in around

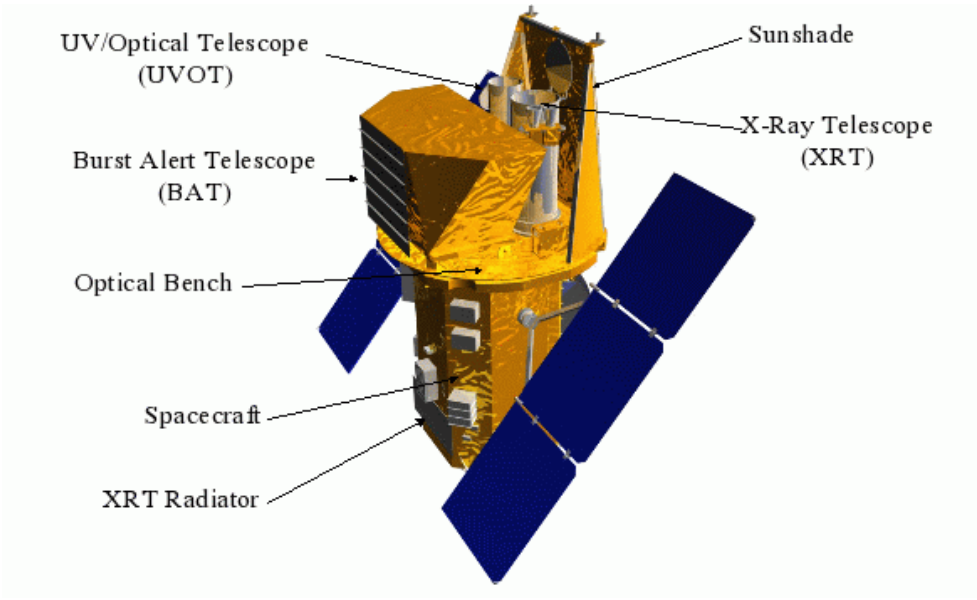

Figure 2.1: Swift and its instruments. (Credit: www.swift.ac.uk)

20–75 seconds, the spacecraft is slewed to point XRT and UVOT to the source.

Each year, Swift observes around 90 GRBs. So far it has observed a total of 1277 GRBs [1] as of late January 2019. All the processed Swift data is made public and available on the web. In January 2018, Swift was named after its recently deceased PI Neil Gehrels. It is still continuing its operations as usual, way after its two-year-long minimum planned life, as of early 2019.

All the information of the mission is obtained from The Swift Technical Handbook version 14.0 [24], and Burrows et. al., 2005 [25].

2.1.1 X-Ray Telescope (XRT)

XRT is an autonomous Wolter-I X-ray telescope with 3.5 m focal length. It has a 600×602 pixel CCD detector, with 23.6×23.6 arcminutes of FoV so that a single pixel corresponds to 2.36 arcseconds. The detector has an energy range of 0.2–10 keV. At 1.5 keV, it has a 15 arcsecond half-power diameter resolution and the effective area of 120 cm^2. Its FWHM energy resolution is 50 eV at 0.1 keV, and 190 eV at 10 keV. It is supposed to be cooled down to -100°C to minimize the internal noise. However,

[1] https://swift.gsfc.nasa.gov/archive/grb_table/stats/ (Accessed on 31 Jan 2019)

as its thermoelectric cooler could not be powered during initiation, XRT is passively cooled, its temperature kept below -50°C. The X-ray mirrors of XRT are actually spare mirrors of the JET-X instrument of *Spektrum-X-Gamma* mission, which was never launched.

XRT has four readout modes, of which only three are currently available. XRT determines itself which mode is suitable for the observation. Imaging (IM) mode creates an image by summing up all the incident photons per pixel, similar to an optical CCD; but this mode cannot be used for spectroscopy. Windowed timing (WT) mode has a 2.2 ms time resolution, creates only a one-dimensional image, yet this mode can be used for spectroscopy for fluxes below 600 mCrab. Photon counting (PC) mode preserves both two-dimensional image and spectrum information, in exchange for reduced time resolution of 2.5 seconds. This mode can be used for fluxes below 1 mCrab, but pileup has to be taken care of, especially for sources with more than 0.5 ct s^{-1}. In this thesis, Swift data taken in PC mode is used. Photodiode (PD) mode is currently unavailable, which was used to create light curves of very bright sources with 0.14 ms time resolution.

2.2 Rossi X-Ray Timing Explorer (RXTE)

Rossi X-Ray Timing Explorer (RXTE) was a space observatory dedicated to X-ray astronomy. Named after the prominent physicist Bruno Rossi (1905-1993), RXTE was launched on 30 December 1995 as a part of the NASA's Medium-class Explorer program (MIDEX). It was placed in low-Earth orbit, where occultation by the Earth itself and the passes through South Atlantic Anomaly (SAA), a region with higher radiation levels, has to be taken into account while performing observations. As in many other space observatories, the position of the Sun was another constraint on observations. There were three scientific instruments on RXTE (Figure 2.2): All Sky Monitor (ASM) had the ability of scanning $\sim$80% of the sky in $\sim$90 minutes and locating a bright transient with $\sim 3' \times 15'$ with its three wide-angle shadow cameras. The ASM data are not proprietary. Proportional Counter Array (PCA) consisted of 5 identical proportional counters, operating at 2–60 keV range. The High Energy X-ray Timing Experiment (HEXTE) consisted of two clusters of four phoswich scintillation

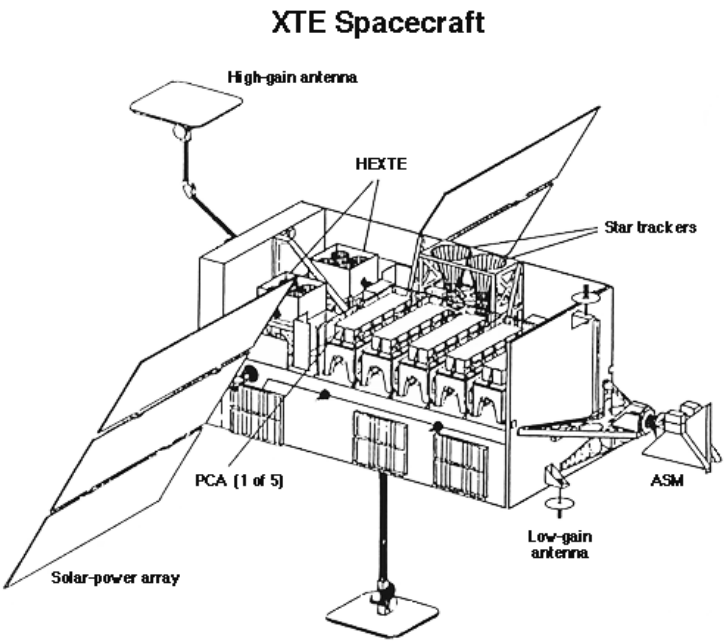

Figure 2.2: RXTE and its instruments. (Credit: NASA)

detectors, operating at 15–250 keV range. PCA and HEXTE both had a FWHM circular FoV of 1° and are co-aligned, therefore they could observe the same object in different energy ranges. The data obtained through an accepted proposal was proprietary for one year, before it becomes public. RXTE had a two-year-long minimum planned life, yet it served 16 years in space. The scientific operations of RXTE were ceased on 3 January 2012, and the spacecraft re-entered the Earth's atmosphere on 30 April 2018.

All the information of the mission is obtained from The XTE Technical Appendix (Appendix F) [26], and Jahoda et. al., 2006 [27].

2.2.1 Proportional Counter Array (PCA)

Proportional Counter Array (PCA) consisted of five identical proportional counter units (PCU). A proportional counter is a device to detect X-ray photons via photoelectric effect. It is filled with some gas (in RXTE PCUs, it is xenon and methane) and a potential difference is applied inside. When the incoming X-ray photons enter a proportional counter, they ionize the gas atoms. The ions are slower to move

because of their mass, whereas the electrons accelerate rapidly towards the cathode and they ionize more atoms while traveling, ultimately creating an ever growing current—this mechanism is called as *Townsend avalanche*. This electrical signal gain is proportional to the energy of the incident photon, therefore the proportional counters can detect the time and the energy of the incoming X-ray photons. Further, the PCUs in PCA also had a collimator and propane layer. The collimators limited the FoV of the PCUs to 1°, but did not focus the incoming photons, therefore PCA provided no images of the pointed sky. And the propane layer acted as an anti-coincidence shield to distinguish high energy particle events. A schematic of the PCU is illustrated in Fig. 2.3.

Each PCU in this instrument had an effective area of $\sim$1300 cm^2, therefore the total effective area of PCA was around 6500 cm^2. The immense size of the detector allowed the instrument to achieve very high count rates: each PCU was able to detect up to 20 000 counts per second. PCU also had a superior 1 µs time resolution (2^{-20} s, to be exact), the energy range of 2–60 keV, energy resolution of %18 at 6 keV and 256 energy channels. The operational temperature range of PCA was -15 to +35°C.

Though the PCUs were identical, they were not working with the same efficiency. Some problems and breakdowns in the PCUs necessitated extra calibrations, such as

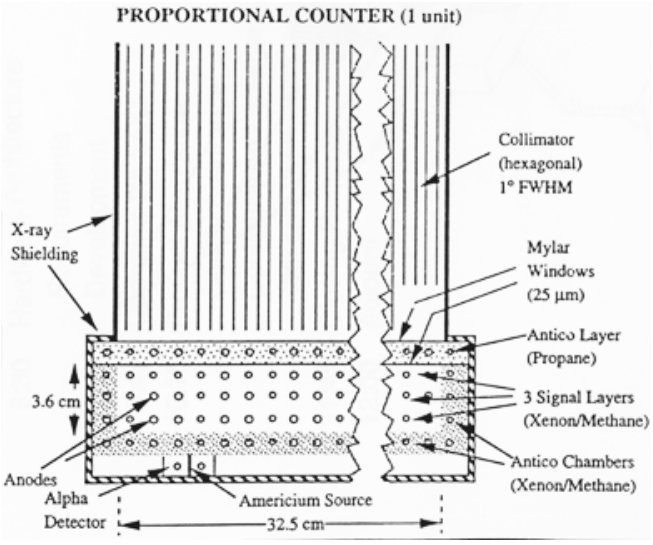

Figure 2.3: A cross-section drawing of a PCU in the Proportional Counter Array. (Credit: NASA)

changing PCU voltages etc. The periods between such main calibrations are called *epoch*s; the last epoch (epoch 5) started on May 2000. The data spanning multiple epochs should be treated carefully as the background rates, gains and energy channels of the data would be different. Moreover, not all PCUs were on all the time, so the count rates should be normalized as if all PCUs were running.

The data created by PCA were handled by Experiment Data System (EDS). It processed incoming PCA data with its six event analyzers (EA) (the other two were dedicated to ASM) using appropriate data "modes". There are seven modes for PCA, namely *binned data*, *pulsar fold*, *delta binned*, *event encoded*, *burst catcher*, *single-bit code* and *Fast Fourier Transform*. Additionally, EAs run two configurations of binned mode for all PCA observations: *Standard-1* mode created light curves with 0.125 second resolution without any energy information. *Standard-2* mode had 16 second resolution and it has 129 energy channels. In this thesis, binned data and event encoded modes are used.

2.3 The Monitor of All-sky X-ray Image (MAXI)

The Monitor of All-sky X-ray Image (MAXI) is a all-sky monitoring mission in X-ray astronomy. Designed by Japan Aerospace Exploration Agency (JAXA), it was launched with the Space Shuttle Endeavour on 16 July 2009. Then it was installed to the Japanese Experiment Module - Exposed Facility (JEM-EF) aboard the International Space Station (ISS), which currently orbits around 405 km above the Earth with a period of $\sim$93 minutes. MAXI monitors $\sim$95% of the sky in X-ray each orbit and any detection of a significant phenomenon is transmitted automatically within 30 seconds. If the MAXI ground system in Japan cannot communicate with MAXI, which occurs the total of a couple hours each day, there will be a delay between 20 minutes to 3 hours. As of early January 2019, there are 31 sources named after MAXI [2].

MAXI has two main instruments—both slit cameras—for X-ray monitoring. Slit cameras only provide one-dimensional position information at a time, but over the

[2] http://134.160.243.88/top/slist.html (Accessed on 12 Jan 2019)

course of a full orbit around the Earth, the cameras are able to scan a large a part of the sky. Both cameras can locate a bright transient with an accuracy better than 0.1°. The cameras are able to detect an X-ray transient with $\gtrsim$80 mCrab in a single scan, or $\gtrsim$8 mCrab for 4 days [28].

Gas Slit Camera (GSC) consists of 12 identical gas proportional counters, with the total effective area of 5350 cm^2. It has the energy range of 2–30 keV and 16% energy resolution at 6 keV. The FoV of GSC is 1.5° (FWHM) × 160°, it is able to scan ∼90–98% of the sky in one full orbit. The instrument's timing accuracy is 120 μs [29] [30].

Solid-state Slit Camera (SSC) consists of two cameras, each has 16 peltier-cooled X-ray sensitive CCD chips. Each CCD has a 1024×1024 pixel resolution, and are cooled down to -60°C. SSC has the energy range of 0.5–12 keV and <0.15 keV energy resolution at 5.9 keV. The total effective area of SSC is 200 cm^2. The FoV of SSC is 1.5° (FWHM) × 90°, it is able to scan ∼70% of the sky in one full orbit. The instrument's timing accuracy is worse than GSC because of the readout time of its CCDs: It is 3 to 16 seconds.

There are also some support instruments. Visual Star Camera (VSC) and Ring Laser

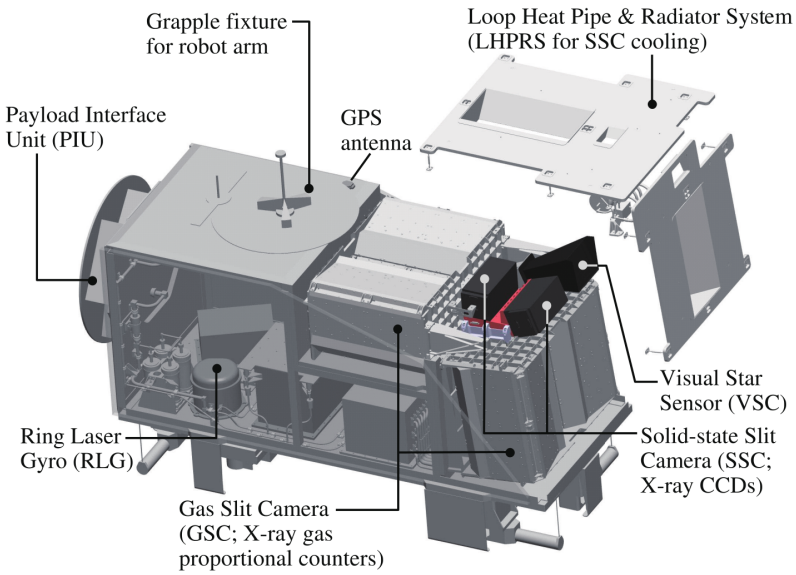

Figure 2.4: MAXI and its instruments. (Credit: Matsuoka et. al. 2009 [2])

Gyroscope (RLG) determines the direction of the cameras, Loop Heat Pipe and Radiation System (LHPRS) cools the CCDs, and a Global Positioning System (GPS) provides precise timing.

The information of the mission is obtained from Matsuoka et. al. 2009 [2], otherwise noted.

CHAPTER 3

THE SOURCE: MAXI J1409-619

3.1 Introduction to the Source

MAXI J1409-619 is a transient HMXB pulsar, most likely a Be type X-ray binary. It was discovered by MAXI/GSC on 17 October 2010, with a (41$\pm$7) mCrab peak flux in 4–10 keV, and the discovery was announced by an ATel on 20 October [31]. On the same day, Swift made a 1 ks target of opportunity (ToO) observation and located the source with 1.9 arcseconds spatial precision at RA = 14^h 08^m 02.56^s, Dec. = -61° 59′ 00.3″ in J2000 coordinates. It was $\sim$0.4° away from the galactic plane and its position did not show up in X-ray object catalog, therefore it was considered as a new X-ray transient. The average flux observed by XRT in 0.3–10 keV was 1.3×10^{-10} erg s^{-1} cm^{-2}. The spectrum was consistent with an absorbed power law fit. Additionally, BAT also detected the source in the 15–50 keV band [32]. Later, on 22–23 October, 7.5 ks of RXTE ToO observations were conducted. $\sim$5 mCrab flux in 2–10 keV energy band was observed; and though there were fluctuations in flux, no meaningful periodic variation was evident. The spectrum could be fitted with a cut-off power law with a reflection, or partially covered power law plus an iron line at (6.5$\pm$0.2) keV with $\sim$0.2 keV equivalent width [33].

After more than a month, on 30 November, Swift/BAT was triggered by an outburst of MAXI J1409-619. The subsequent 2 ks XRT observation with both PC and WT modes showed that the source became $\sim$7 times brighter than when it was first observed, with an average flux of 7×10^{-10} erg s^{-1} cm^{-2} in 0.3–10 keV. Moreover, an X-ray periodicity was detected in the source for the first time: A (503$\pm$10) s period with 42% sinusoidal peak-to-through modulation in the pile-up corrected PC mode

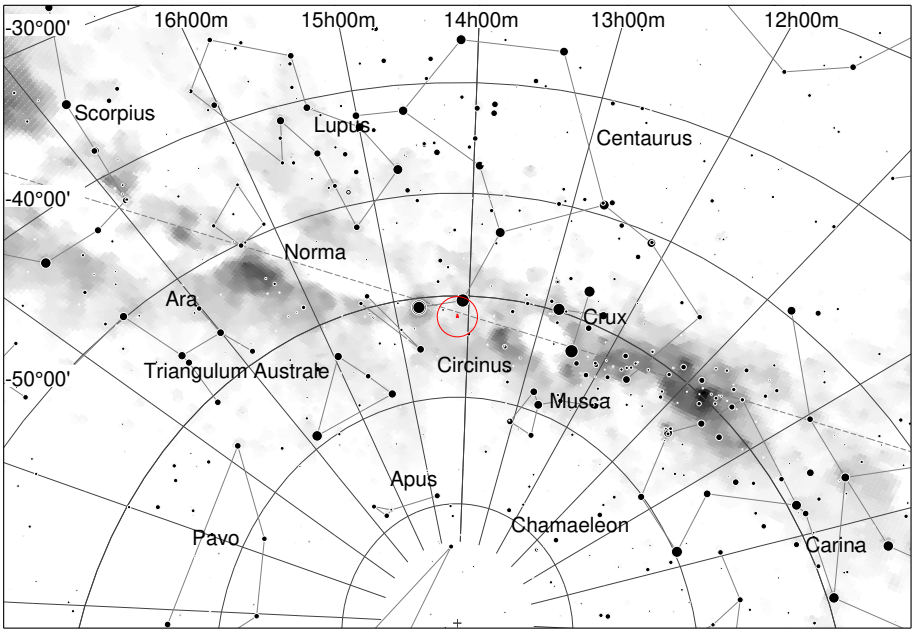

Figure 3.1: Location of MAXI J1409-619 in the sky. (Image from Cartes du Ciel)

data [34]. Routine MAXI/GSC observations indicated that the source was brightened significantly between 25 November–3 December [35]. Similarly, Fermi Gamma-ray Burst Monitor (GBM) determined a similar period of 506.93(5) s using its observations on 2–3 December. The rate of change in the frequency $\dot{\nu} = 1.66(14)\times10^{-11}$ Hz/s between 2–5 December and the double-peaked nature of the pulse profile was also reported [36] [1]. 8.5 ks XTE observations on 4 December also confirmed the periodicity. A (506$\pm$1) s period and $\sim$8$\times10^{-10}$ erg s^{-1} cm^{-2} ($\sim$33 mCrab) flux in 2–10 keV band were determined using those observations. The PCA spectrum was fitted by a cut-off power law with a partially covered absorption, or a reflection and a narrow iron line. In both fits, the photon index was found to be $\Gamma \approx 1.3$; and they found no sign of cyclotron absorption. So far, MAXI J1409-619 was already identified as a long-period HMXB Be pulsar.

After continuous observations throughout December, Kaur et. al. announced the detection of a QPO with 2 harmonics using a total of 20 ks of observations [37]. It was the first detection of QPO harmonics in an accreting pulsar [38]. The main QPO was

[1] The relevant Fermi data and plots are available at https://gammaray.msfc.nasa.gov/gbm/science/pulsars/lightcurves/maxij1409.html (Accessed on 5 Dec 2018)

found to be at (0.192±0.006) Hz with (0.029±0.013) Hz width, 5.0 σ significance. Moreover, harmonics are found at (0.422±0.012) Hz with (0.047±0.036) Hz width, 5.5 σ significance; and at (0.621±0.018) Hz with (0.076±0.070) Hz width, 3.6 σ significance. $\nu_{QPO}/\nu_{spin} \approx 96$ ratio was the greatest among the known HMXBs. They calculated the QPO producing region of the source to be around 5000 km, assuming 1.4 $M_{\odot}$ star mass. They fitted the PCA spectrum with a cut-off power law plus a narrow iron line, where Γ =(0.90±0.02) and e-folding energy = (19.9±0.9) keV [37].

Archival observations covering the position of MAXI J1409-619 were also examined for a possible pre-discovery recovery. BeppoSAX observations between 1997–2000 made a faint detection at the position of the source. One ASCA observation in 1998 covering the region around MAXI J1409-619 also detected a source. On the other hand, a total of ∼2.3 Ms observations of INTEGRAL had not made a significant detection. The results inferred that MAXI J1409-619 was at a low state during that period and it is most probably an accreting pulsar [39, 40].

3.2 Observations of The Source

This thesis includes Swift and RXTE observations of MAXI J1409-619. A summary of the used observations are in Table 3.1 below:

Table 3.1: Summary of MAXI J1409-619 observations.

Satellite	# of obs.	Start date	End date	Total obs. duration (s)
Swift	15	20 Oct 2010	28 Jan 2011	19 265
RXTE	50	22 Oct 2010	5 Feb 2011	135 045

3.2.1 Swift XRT

Swift XRT made 32 observations of MAXI J1409-619 between 20 October 2010 and 28 January 2011, with a total exposure of 43.5 ks. Of these observations, 13 of them are in photon counting (PC) mode, 17 of them are in window timing (WT) mode and

2 of them utilizes both modes. Only the observations having PC mode data are used, with a total exposure of 19.3 ks.

XRT observations began when the source was discovered, and continued until 3 November. All but 2 observations were recorded in PC mode. After a 27-day-long gap, observations resumed by the BAT trigger of outburst on 30 November, and continued throughout the outburst fade out until 28 January next year. These observations started in PC mode, but switched to WT mode to better handling of higher flux. The last 4 observations were reverted to PC mode again, as the flux had waned enough.

Table 3.2: List of Swift XRT observations. The observations are grouped into 6 groups for the spectral analysis.

ObsID	Group no	Date	Date (MJD)	Exposure (s)
31850001	1	2010-10-21	55490	1897
31850002		2010-10-22	55491	1692
31850003	2	2010-10-23	55492	1667
31850005		2010-10-25	55494	1638
31850007	3	2010-10-28	55497	1176
31850008		2010-10-30	55499	935
31850009	4	2010-11-01	55501	843
31850010		2010-11-03	55503	1208
439550000	5	2010-11-30	55530	1748
31850011		2010-12-01	55531	850
31850027	6	2011-01-16	55577	1208
31850028		2011-01-19	55580	1231
31850029		2011-01-22	55583	1318
31850030		2011-01-28	55589	857

3.2.2 RXTE PCA

RXTE PCA made 51 observations of MAXI J1409-619 between 22 October 2010 and 5 February 2011, with a total exposure of 136.5 ks. All but one observations are used, with a total exposure of 135.0 ks.

There are three groups of PCA observations. The first group observations were between 22 October and 4 November, when the count rates were relatively lower;

and two observations on 4 December, just after the outburst. The second group of observations were between 10 December and 30 December. These observations cover the peak of the outburst, and daily observations are done during this period. The last group of observations were done between 5 January and 5 February next year, when the outburst had mostly faded. The time intervals between these observations are larger. The last two group are ToO observations.

Table 3.3: A summary of RXTE PCA observations. # denotes the number of observations. The complete list of observations are at Appendix A, Table A.1.

Proposal no.	#	Date range	Date (MJD)	Exposure (s)
95358	16	2010-10-22 – 2010-12-04	55491–55534	37794
95441	22	2010-12-10 – 2010-12-30	55540–55560	74388
96410	12	2011-01-05 – 2011-02-05	55566–55597	22863

CHAPTER 4

DATA ANALYSIS AND RESULTS

All data processing and analysis were conducted in *HEASOFT 6.22.1*. Spectrum and light curve analysis of Swift and RXTE data uses the same tools, i.e. *xspec* and *lcurve*, but reprocessing the raw/preprocessed data is done using different steps and tools.

4.1 Data Preparation

4.1.1 Swift XRT Data

To prepare Swift XRT data for analysis, the raw data are first reprocessed with the pipeline command *xrtpipeline*. Using the event files from all observations, an image is extracted with *xselect*. In *ds9*, a circular region of 20 pixel radius centered on the source is selected for the source events; and another arbitrary one with 50 pixel radius is selected for background events. As the count rates exceed $\sim$0.5 counts s^{-1}, pile-up correction is done.

For spectral analysis, PHA (pulse height amplitude) files are created with *xselect* for source and background regions. There are some bad pixels and bad columns in the XRT CCD sensor, therefore an exposure map should be created with *ximage* and *fparkey* to compensate the irregularities. Then, an ARF (ancillary response file) is created with *xrtmkarf* for determining the effective area of the CCD in various photon energies. Lastly, with *grppha*, the source PHA file is modified: Relevant ARF, RMF and background filenames are added as keywords; first 30 channels (corresponding below 0.3 keV) of the data are marked as "bad" because XRT data are not reliable below this threshold; and spectrum binning is done in such a way that there are at

least 20 counts per bin, which is necessary for χ^2 fitting. The final PHA file is ready for spectral analysis in *xspec*.

For the light curve analysis, source and background light curve file are extracted separately with *xselect* using previously created source and background regions. If desired, a filtering command can be added to include only the desired range of channels. Afterwards, the resulting light curve is background-subtracted with *lcmath*, and barycentric correction is done with *barycorr*.

4.1.2 RXTE PCA Data

In RXTE PCA data analysis, *Standard-2* is used for spectra and *Good Xenon* mode is used for light curves. Timing resolution is 16 seconds in Standard-2 mode, and 2^{-20} seconds ($\sim$1μs) in Good Xenon mode. PCA data does not give an image and includes all the information inside the FoV, but fortunately there are no other sources nearby so that the data are not contaminated by other X-ray sources. The necessary file lists are created with *xdf*, and good time intervals are created for filtering with *maketime*. To satisfy the good time interval requirements, the elevation angle between Earth's limb and the source should be greater than 10° (otherwise the atmosphere will absorb the incoming X-rays), and pointing of the instrument and the source position should not differ more than 0.02° (at the beginning and the end of the observations, slewing might be an issue), and electron contamination on PCU 2 should be less than 0.1.

For light curve analysis, Good Xenon data from two EAs are combined with *make_se* first. The light curves are extracted with 0.125 second bin size with *seextrct*. Then, the suitable background model is applied to Standard-2 data with *runpcabackest* for background estimation. Bright background model is used when the net count rate is greater than 40 counts per second per PCU, which is the case for all but the latest observations, and faint background model is used otherwise. Both background models are available at HEASARC website for direct use. Using the output, background light curves are created with *saextract*, and subtracted by *lcmath* to eliminate the background events. As PCUs may turn on and off during observations, the light curves are normalized with *correctlc* as if all PCUs were working. Lastly, the barycentric correction is done with *fxbary*.

For spectral analysis, only the data coming from PCU 2 are used. The PHA spectra are created with *saextract*. Using the suitable background model, background estimation is done and background PHA spectra files are created. Using *pcarsp*, RMF response files are created, and with *grppha*, the background filenames are added as keywords in the source PHA spectra. The resulting file is ready to be analyzed in *xspec*.

4.2 Light curves

Using both Swift and RXTE data, light curve plots covering all observations are created (Figure 4.1). These light curve plots show the timing and outburst coverage of the observations of both satellites. Swift PC mode data have a huge gap, whereas RXTE data cover all the phases of the outburst. Nevertheless, both light curves correlate closely in terms of the count rates.

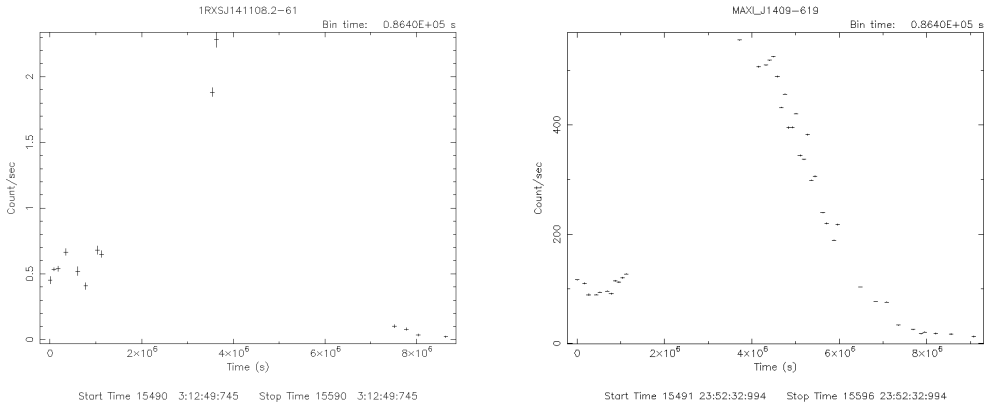

Figure 4.1: Swift (left) and RXTE (right) light curves with one day bins.

Though more detailed QPO and phase-bin analysis are done with the light curves, the light curves covering single observations are created and visually inspected in addition. The first light curves seem to fluctuate randomly, but the periodicity in the light curves after the outburst is evident (Figure 4.2).

On 17 Dec 2010 (MJD 55547), while the outburst is fading, a short outburst and exponential decay totaling $\sim$10 seconds is found. The count rate of the peak is around 4 times of the regular peak count rates of that observation (Figure 4.3).

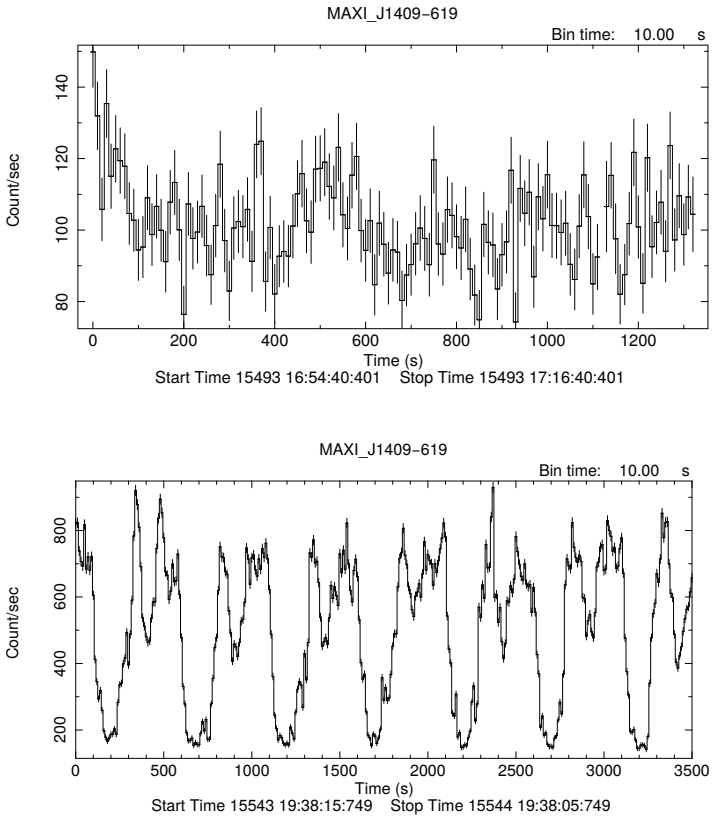

Figure 4.2: The RXTE lightcurves from 24 Oct 2010 / MJD 55493 (top) and 13 Dec 2010 / MJD 55543 (bottom).

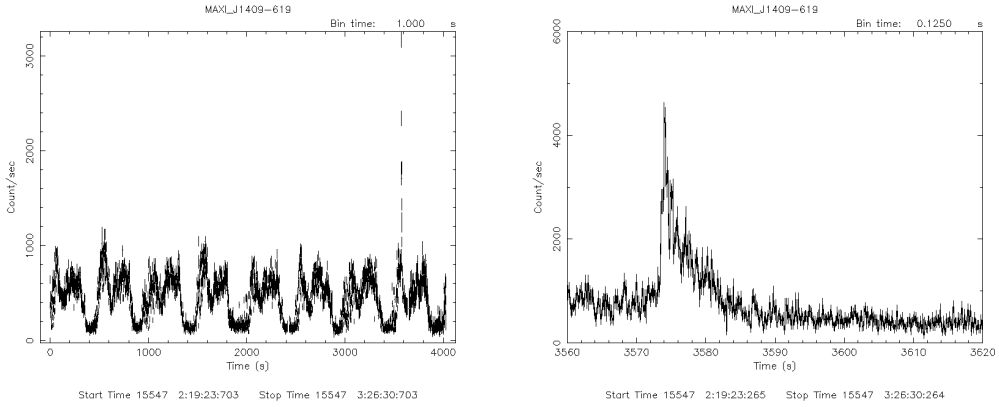

Figure 4.3: The small outburst detected on 17 Dec 2010 / MJD 55547. The light curve covering all the observation is on the left, the zoomed-in light curve is on the light.

4.3 Spectral Analysis

4.3.1 Swift

Swift XRT has a moderate resolution in spectrum analysis, nevertheless the observations are used for spectral analysis. Furthermore, no single observation proceeds more than 2 ks. Such limited exposure times are not sufficient to obtain convenient results by spectral analysis. For this reason, observations are combined into six groups in order to increase the statistical significance of the results (see Table 3.2). Being close in time and having similar count rates are the main criteria for combining the observations into the same group.

The spectra are binned with a minimum of 5 counts per bin, and C statistic (*cstat*) is used in *xspec*. The spectra are fitted simply with a photoelectric absorption $\times$ power law (*phabs*powerlaw*) model. The 90% confidence ranges of the fit parameters are calculated with *uncer* ("*uncertain*", same as *error*) command. The flux of the entire model is calculated with the command *cflux*. To calculate hardness ratios, the fluxes in 0.3–4.0 keV and 4.0–10.0 keV and their confidence ranges are calculated as well. A fitted spectrum example and the fit parameters are added below (Figure 4.4, Figure 4.5, Table 4.1). All spectrum plots are presented in Appendix B.

Table 4.1: Spectra fitting parameters of Swift XRT data. Note that flux values are in terms of 10^{-10} erg s^{-1} cm^{-2}.

	Group 1	Group 2	Group 3	Group 4	Group 5	Group 6
Obs. midtime (MJD)	55490.89	55493.19	55498.34	55502.52	55530.86	55583.68
$\sum$duration (s)	3590	3305	2111	2051	2597	4615
n_H ($\times 10^{22}$ cm^{-2})	$5.43^{+0.74}_{-0.66}$	$3.78^{+0.98}_{-0.86}$	$2.99^{+1.11}_{-0.96}$	$5.35^{+1.65}_{-1.41}$	$5.21^{+0.63}_{-0.59}$	$9.08^{+4.44}_{-3.47}$
Photon index	0.73	$0.73^{+0.32}_{-0.31}$	$0.30^{+0.36}_{-0.35}$	$1.03^{+0.46}_{-0.43}$	$0.89^{+0.18}_{-0.18}$	$1.78^{+1.00}_{-0.90}$
Hardness ratio	2.29	2.28	3.80	1.56	1.86	0.48
Flux	$1.38^{+0.12}_{-0.11}$	$1.17^{+0.10}_{-0.10}$	$2.02^{+2.64}_{-1.11}$	$1.68^{+0.19}_{-0.17}$	$8.61^{+0.40}_{-0.39}$	$0.13^{+0.06}_{-0.03}$
Reduced χ^2	1.0615	1.1150	0.9286	0.7237	0.99558	1.163

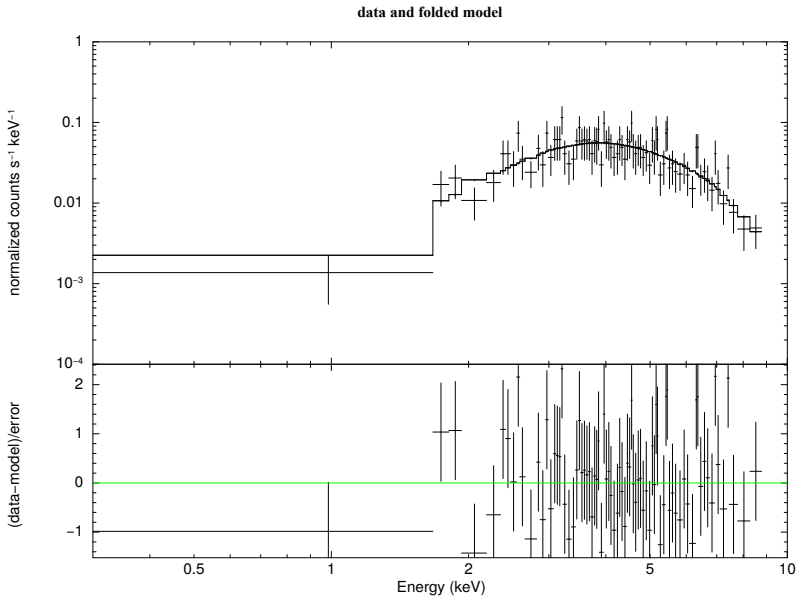

Figure 4.4: Swift XRT spectrum of MAXI J1409-619 with power law model (Group 4, MJD 55501–55503).

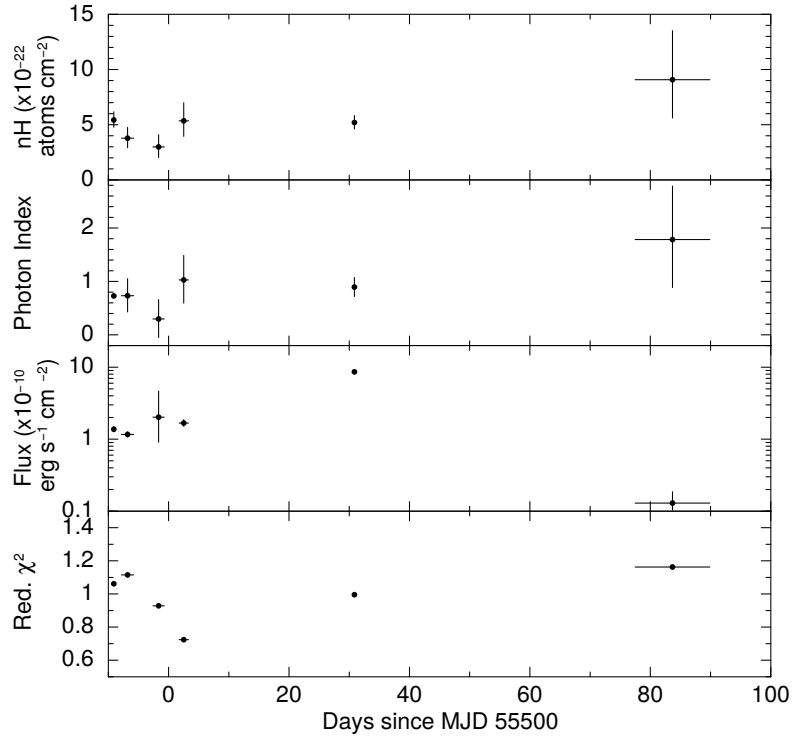

Figure 4.5: The fitting parameters of Swift XRT observations over time.

The given model is successful at fitting the spectra. The reduced chi-squared statistic values of the fits are between 0.72 and 1.21. In group 3 observations, bad rows in each observation overlap very close to the center of the source, which may deteriorate the count rates and the results. In group 3 and 6, pile-up correction is not found to be necessary and is not done. In group 1, the photon index parameter is fixed as setting all parameters free does not gave reasonable results. It is fixed at 0.73, which as taken from the group 2, which is close in time and count rates to group 1.

4.3.2 RXTE

We begin RXTE PCA spectral analysis by combining and fitting all observations in 95441 set (74.4 ks) as a whole. Different models are tested on the spectrum to find out the most suitable model for further analysis. Then, all observations are analyzed separately. Subsequent observations are combined when total durations of the observations are not sufficient enough for obtaining statistically significant results. For all fitting in RXTE, 3.0–25.0 keV range is selected, and fluxes are determined with *cflux* command.

4.3.2.1 Overall Spectra

The observations of the 95441 set span around one month and a wide range of the outburst, the resulting spectrum rather gives a general idea about the nature of the source. While 95441 set is fitted as a whole, a systematic error of 0.5% is set. Among the different models, power law with a high energy cutoff plus a Gaussian iron line fixed at 6.4 keV, all combined with photoelectric absorption gives the most plausible results (*phabs*(cutoffpl+gauss)*, Figure 4.6). Later on, 96410 set is similarly fitted as a whole as well.

4.3.2.2 Time-Resolved Spectroscopy

In order to investigate the evolution of the fit parameters over time, the observations are fitted separately. When the exposure times are sufficient, the single observations

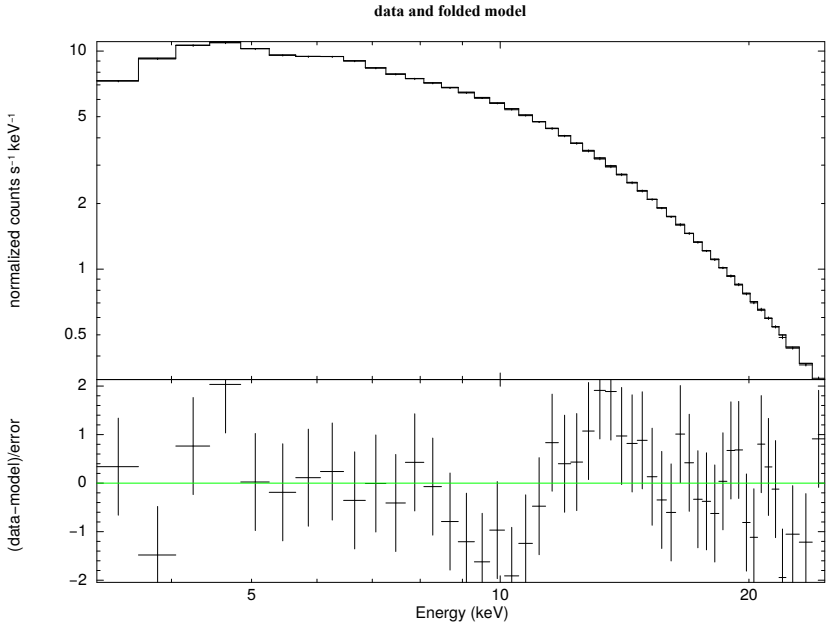

Figure 4.6: RXTE PCA spectrum of 95441 set (MJD 55540–55560, 74.4 ks) is best fitted with power law with a high energy cutoff plus a Gaussian iron line fixed at 6.4 keV.

are used; otherwise, subsequent short observations are combined before fitting. Most of the spectra are fitted with a cutoff model. However, as the count rates of the observations decrease, increasing signal-to-noise ratios deteriorates the spectral quality, causing difficulties in finding cutoff energies. Therefore some spectra are fitted with a power law model, which is statistically simpler than the cutoff model. Additionally, a 0.5% systematic error is set while fitting some spectra of combined or long-duration observations.The evolution of the fit parameters over time are presented at Figure 4.7. All time-resolved spectra are presented in Appendix C.

The selected models accurately fit the spectra: Only two spectra has χ^2 values larger than 2. Despite that, a bump around 10 keV is seen in fit residuals, especially in long observations. This feature is mentioned in Coburn et. al [41]. It was observed in many accreting X-ray pulsars, not only in RXTE but also Ginga and BeppoSAX. Always around at 10 keV, the feature is not thought be a cyclotron line or another absorption feature, therefore it was concluded that it might be an innate feature common in accreting pulsars. Using NPEX model is considered as a possible workaround, none-

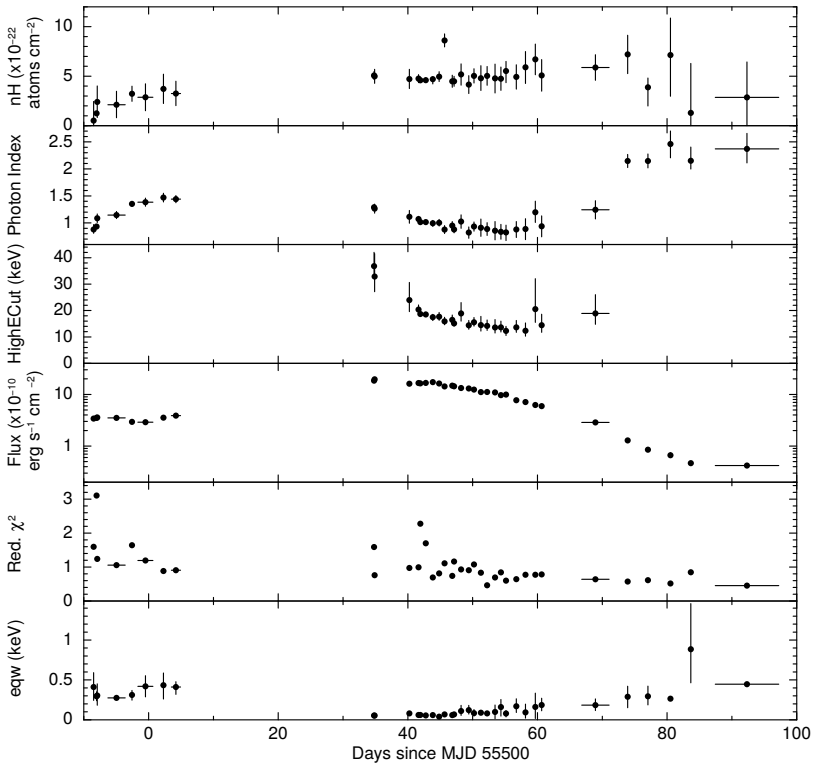

Figure 4.7: The fitting parameters of RXTE PCA observations over time.

theless it is not completely successful at eliminating the feature.

The evolution of the photon index over time is a little bit complex. At the beginning, there seems to exist a slight anticorrelation between the photon index and the count rates: The emission softens to a limited extent after the initial detection of the source. This part is not of particular interest as the outburst stage is examined more thoroughly. Then, at the outburst stage, the photon index slightly decreases with decreasing flux. However, after passing a point of decreasing flux, the photon index increases rapidly and it is at its maximum with minimum flux. Photon indices versus fluxes are plotted in Figure 4.8. With increasing flux, the photon index decreases; in other words, the emission is hardened. However, beyond some threshold of flux, photon index stays flat. As the flux is directly related with the mass accretion rate, it might be argued that photon index is insensitive to the mass accretion rate after passing a threshold point. Only around the maximum flux, the photon index tends to increase slightly.

High energy cutoff values are only obtained at the outburst stage, and is decreasing

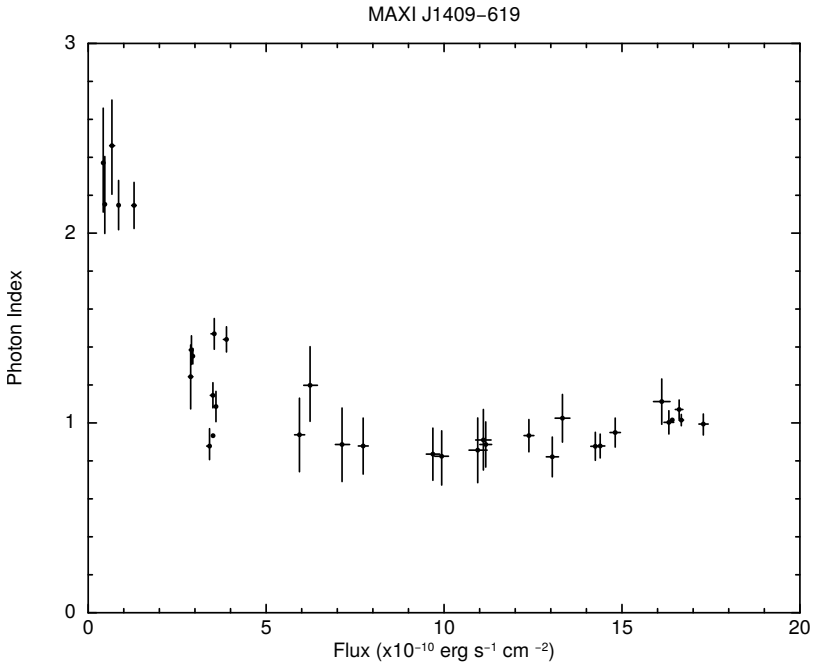

Figure 4.8: The relation between photon indices and fluxes of RXTE PCA observations.

over time. At the pre-outburst stage and the tail of the outburst, statistically meaningful cutoff values cannot be found.

4.3.2.3 Phase-Resolved Spectroscopy

When the spin period of a source is known, it is possible to split and bin the data in different phases of the spin, and create spectra for each phase to analyze the changes throughout the spin.

For phase-resolved spectroscopy, 3 observations on 11–12 December 2010 (MJD 55541–55542) totaling 34.0 ks are used, where the outburst is at its maximum. To find the spin period of the object, *efsearch* command is used on the relevant light curve. The spin period during that time is found to be 503.62 seconds (1.9856 mHz). Using *fasebin*, PHA spectra for different phases are created. A total of 10 phase bins are used; as a result, each spectrum has around 3.4 ks of exposure, which is found to be sufficient for statistically meaningful analysis. A histogram of counts-per-phase-

bin, i.e., a pulse profile is produced with *fbssum*. Moreover, with *fbssum*, an energy-resolved pulse profile can be produced to see the pulse variations in different energy ranges. Finally, the phase resolved spectra are fitted with *xspec*. Originally, these steps were done separately for the data taken on MJD 55541 and 55542; but the results were very similar. Therefore, all the observations are merged and analyzed at once.

The phase resolved spectra are fitted with a high energy cutoff plus a Gaussian iron line. The Gaussian line is fixed at 6.4 keV as usual. The results obtained using this model show similarity with the ones in time-resolved spectra in Section 4.3.2.2. The model described above is generally in good agreement with the spectrum in each phase bin.

The pulse profile is double-peaked (see panel 1&2 of Figure 4.9a). This double peak structure is more evident when the pulse profile is constructed with a larger number of phase bins. As an example, a pulse profile with 40 phase bins is shown in Figure 4.9b. The neutral hydrogen column density n_H does not have a significant variation with changing phase. The photon index appears to be lower during the peaks, and goes up notably when the flux is minimum (Figure 4.9a, panel 3). Higher photon index values at the minimum flux can be explained by hard emission of the pulsed flux. When the pulsed flux diminishes, the observed emission is softened. At the pulse minima, the high energy cutoff value goes out of 3–25 keV range (Figure 4.9a, panel 4). This is probably the result of the increased signal-to-noise ratios due to decreased count rates of the source. Besides, the phase bins corresponding to the pulse minimas have larger χ^2 values, possibly owing to the excess high-energy cutoff values obtained by the fit and the larger signal-to-noise ratios as explained above (Figure 4.9a, panel 5). Lastly, as the count rates dip, the equivalent width of the Gaussian line increases (Figure 4.9a, panel 6). Broadening of the Gaussian line might be explained by blending of two iron lines at pulse minimum: When the enhanced emission of the hot spots fades from view, Kβ line emission at 7.04 keV emerges alongside the Kα line emission at 6.4 keV, resulting the aforementioned broadening [42].

In addition to the pulse profiles in Figure 4.9a, normalized energy-resolved pulse profiles are created, as shown in Figure 4.10. Apparently, the variations in flux

with phase are most prominent in 8-13 keV range, whereas this flux variation largely vanish above 25 keV.

4.4 QPO Analysis

For the QPO search in RXTE data, *powspec* tool is used to create power spectra from the light curves. During the power spectrum generation, the light curves are divided into 128 second long time intervals, each of which contains 1024 bins with 0.125 second rebinning time. Each consecutive 16 intervals are averaged into one frame, therefore each power spectrum plot spans 2048 seconds, i.e., the observations

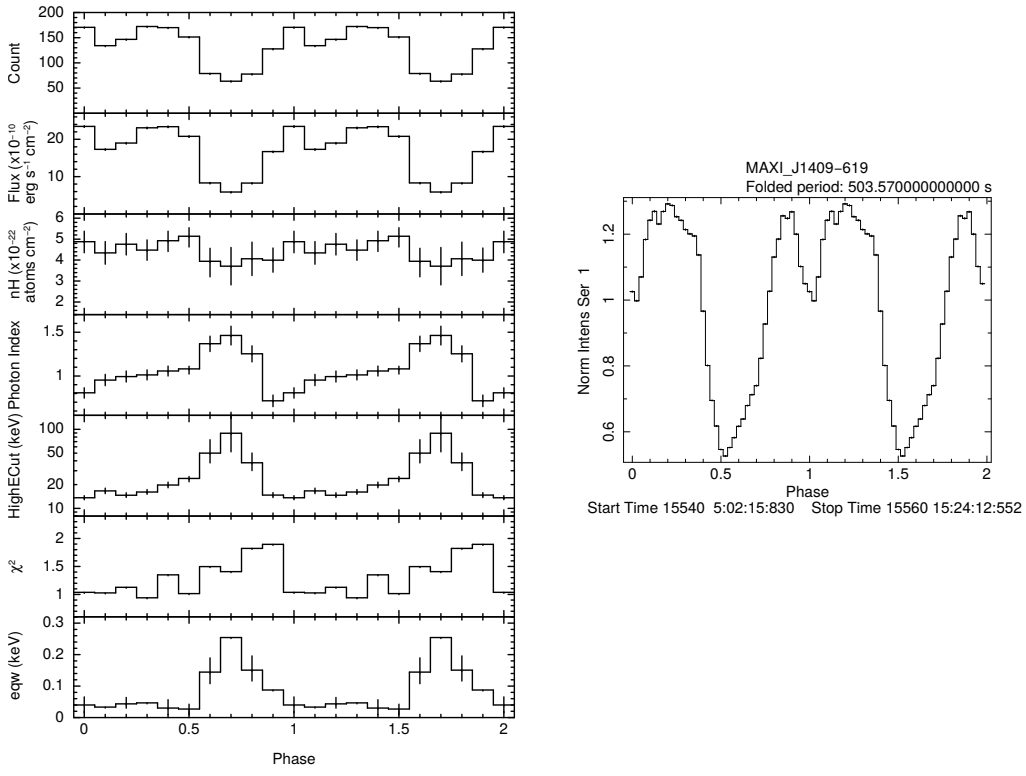

(a) (b)

Figure 4.9: Fitting parameter evolution of RXTE PCA observations in MJD 55541–55542 with changing phase (a). Pulse profile with RXTE PCA observations in MJD 55540–55560, folded using a 503.57 s period and 40 bins (b).

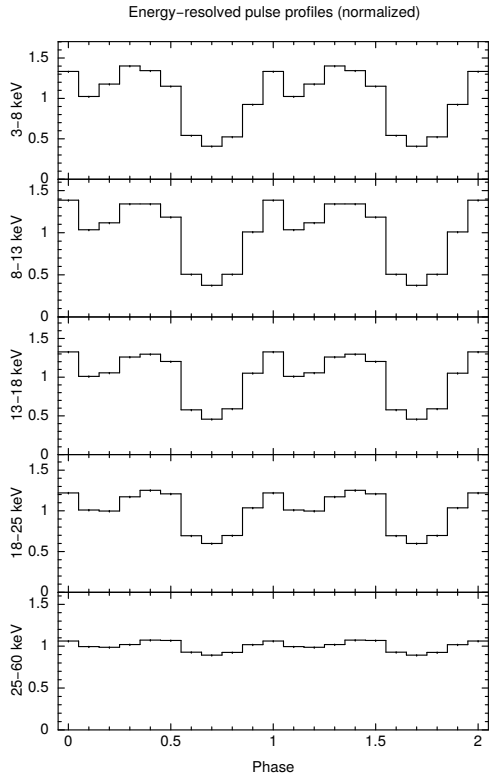

Figure 4.10: Normalized energy-resolved pulse profiles of RXTE PCA observations in MJD 55541–55542.

are split into 2048-second segments for the QPO analysis. If the frame duration is shorter than 2048 seconds (e.g. observations shorter than 2048 seconds, or the last parts of the long observations), we generate the power spectra using the maximum number of frames available corresponding to the total duration of the observation. The results are geometrically rebinned by -1.02 value so that the bins have similar sizes in logarithmic plots.

We developed a Python based code to fit and analyze the resulting power spectra [1]. With this code, the continuum of the power spectra are represented by a smoothly broken power law model. This model is more flexible in smoothing the two ends of the power law slopes, yielding better results when compared to the broken power law

[1] The Python code is written in collaboration with Muhammed Miraç Serim.

model. Smoothly broken power law is defined as

$$f(x) = A\left(\frac{x}{x_b}\right)^{-\alpha_1}\left\{\frac{1}{2}\left[1+\left(\frac{x}{x_b}\right)^{\frac{1}{\Delta}}\right]\right\}^{(\alpha_1-\alpha_2)\Delta} \tag{4.1}$$

where A is the amplitude, x is the frequency, x_b is the break frequency, α_1 and α_2 are the power law indices at frequency $f < x_b$ and $f > x_b$, respectively, and Δ is the smoothness parameter [43]. The QPOs are seen as excess peaks in the continuum and can be modeled as Lorentzian components added to the base continuum model. The additive Lorentzian component is defined as

$$L = \frac{l_n}{1+\left(2\times\dfrac{x-l_c}{l_w}\right)^2} \tag{4.2}$$

where x is the frequency, l_n is the line normalization parameter, l_c is the center frequency of the line, and l_w is the line width [44]. When harmonic peaks of QPO frequency are present, they are also modeled with additional Lorentzian components, represented by Equation 4.2.

The fitting procedure of the power spectra is conducted with *curve_fit* tool. The tool resolves the optimal parameters for the fit and returns the error range of the parameters within one σ level. Comparing the χ^2 values of the fits with and without a Lorentzian, the significance of the QPO component are computed by F-test statistic with the Python package *PyAstronomy 0.12.0* [45]. The power spectra fits of each frame with corresponding QPO sigma values are represented in Appendix D.

QPOs are detected only at the first half of the outburst stage. In the pre-outburst observations, and when the outburst was mostly faded, no QPOs are detected. Time evolution of QPO centroid frequencies, as well as their significance is shown at Figure 4.11. Even if the QPO detections are not significant, they are included in Figure 4.11 in order to keep track of the time evolution of the centroid frequencies. QPO amplitudes fluctuate substantially over time, and QPO components do not always appear. QPO harmonics seem to appear for the most cases, though many of these harmonics are not statistically significant. Even more, at the peak of the outburst, few

instances of second harmonics of QPOs are observed.

Another notable finding is about the QPO centroid frequencies: They decrease consistently over time. The first QPOs are detected around 0.2 Hz; however, as the outburst

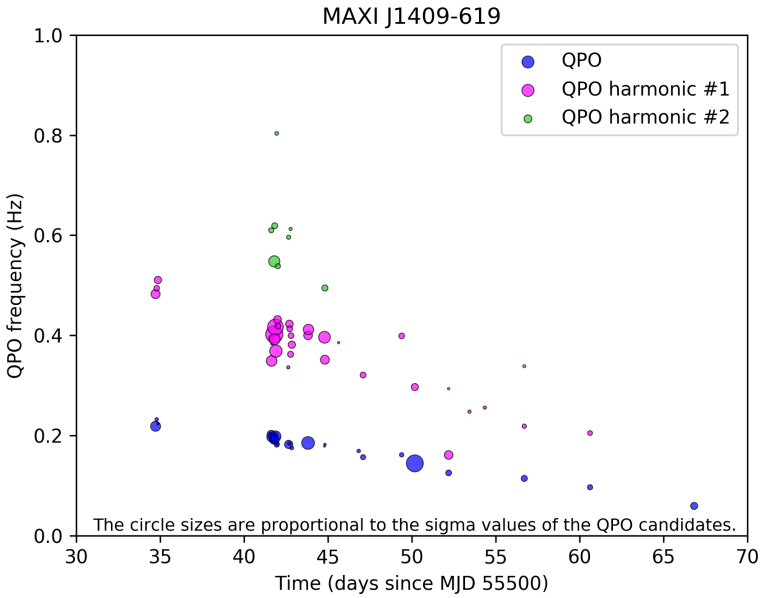

Figure 4.11: QPO centroid frequencies versus time.

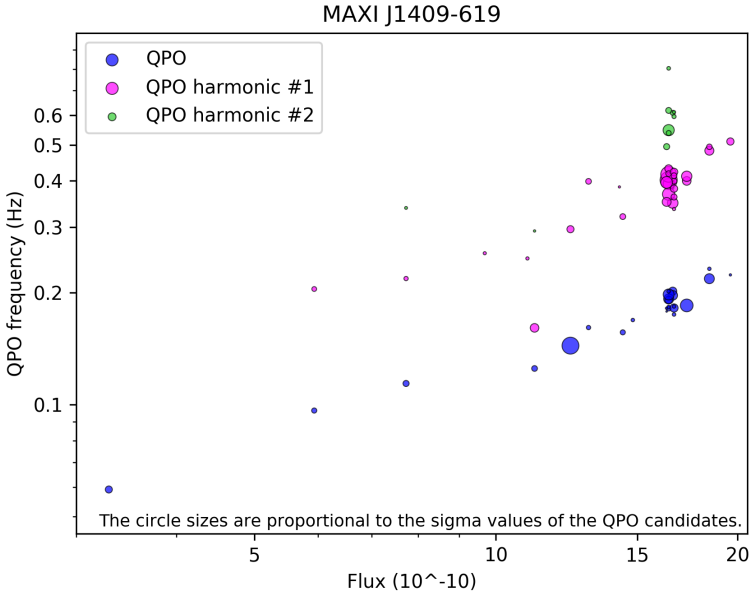

Figure 4.12: QPO centroid frequencies versus flux.

Table 4.2: Detected QPOs.

Epoch	ν_{QPO} (Hz)			Q-factor			Significance (σ)		
(MJD)	#1	#2	#3	#1	#2	#3	#1	#2	#3
55534.729	0.218±0.002	0.482±0.010	-	9.61	9.65	-	2.37	2.15	-
55534.797	0.232±0.006	0.494±0.004	-	5.44	18.38	-	0.82	1.32	-
55534.868	0.223±0.003	0.510±0.020	-	11.06	6.85	-	0.55	1.73	-
55541.621	0.202±0.006	0.395±0.011	0.610±0.019	3.28	19.75	21.76	1.92	1.24	1.19
55541.645	0.197±0.002	0.349±0.005	-	6.62	6.98	-	2.29	2.52	-
55541.804	0.193±0.002	0.402±0.007	0.548±0.018	6.42	8.04	10.95	2.38	4.08	2.66
55541.827	0.191±0.003	0.392±0.010	0.619±0.017	6.38	7.85	12.38	1.80	2.64	1.40
55541.875	0.198±0.003	0.417±0.016	-	3.81	4.17	-	2.61	3.75	-
55541.899	0.202±0.005	0.369±0.015	-	4.64	3.69	-	0.84	2.94	-
55541.948	0.181±0.005	0.420±0.011	0.803±0.056	6.29	30.31	7.72	1.14	0.58	0.87
55541.997	0.183±0.0004	0.432±0.010	-	25.10	8.63	-	0.89	1.83	-
55542.021	-	0.419±0.015	0.538±0.013	-	7.34	22.04	-	1.35	1.20
55542.662	0.182±0.003	-	0.596±0.040	6.27	-	28.58	1.96	-	0.98
55542.705	0.184±0.001	0.423±0.021	-	12.13	7.04	-	0.83	1.80	-
55542.776	-	0.362±0.011	0.612±0.023	-	6.03	12.25	-	1.43	0.75
55542.849	0.175±0.009	0.381±0.011	-	1.75	7.63	-	0.84	1.73	-
55543.818	0.185±0.001	0.400±0.009	-	8.77	6.66	-	3.02	2.06	-
55543.842	-	0.412±0.014	-	-	13.72	-	-	2.46	-
55544.798	-	0.396±0.008	-	-	7.92	-	-	2.79	-
55544.822	0.182±0.004	0.351±0.010	0.495±0.012	5.61	7.86	13.88	0.59	2.12	1.44
55546.835	0.169±0.002	-	-	4.06	-	-	0.83	-	-
55547.097	0.156±0.001	0.321±0.004	-	11.63	12.22	-	1.21	1.38	-
55549.395	0.161±0.001	0.399±0.011	-	8.06	13.92	-	1.03	1.36	-
55550.182	0.144±0.002	0.296±0.012	-	3.60	5.93	-	4.02	1.69	-
55552.197	0.125±0.003	0.161±0.004	0.293±0.010	16.98	3.22	5.87	1.37	2.05	0.56
55556.705	0.114±0.001	0.218±0.009	0.338±0.027	12.33	7.66	16.91	1.45	1.02	0.69
55560.624	0.096±0.001	0.205±0.009	-	7.51	50.76	-	1.23	1.14	-
55566.830	0.059±0.002	-	-	1.86	-	-	1.68	-	-

flux decays, QPO centroid frequencies decrease down to 0.1 Hz. In the time period where the QPOs are detected, the source flux consistently decreases over time as well. Therefore, a relation between the QPO centroid frequencies and the flux can be established, which is shown at Figure 4.12. The figure shows that the QPO centroid frequencies decrease with decreasing flux.

In addition to QPO analysis in many time windows, another QPO analysis is done covering two observations on 11 December 2010 (MJD 55541), when the outburst is at its peak. These observations (19.0 ks) contain many of the significant QPOs, and analyzing the whole data provides better results than splitting it into many segments. Furthermore, the discovery of the QPO feature of MAXI J1409-619 was previously reported by the analysis of the observations in the mentioned time interval [37, Kaur

Table 4.3: QPO parameters of the observations in MJD 55541.

		Results	Kaur et. al. [37]
QPO	$f_{centroid}$ (Hz)	0.190 ± 0.001	0.192 ± 0.006
	f_{width} (Hz)	0.038 ± 0.004	0.029 ± 0.013
	Significance (σ)	3.96	5.0
QPO harmonic #1	$f_{centroid}$ (Hz)	0.405 ± 0.006	0.422 ± 0.012
	f_{width} (Hz)	0.080 ± 0.021	0.047 ± 0.036
	Significance (σ)	5.44	5.5
QPO harmonic #2	$f_{centroid}$ (Hz)	0.618 ± 0.025	0.621 ± 0.018
	f_{width} (Hz)	0.100 ± 0.080	0.076 ± 0.070
	Significance (σ)	2.40	3.6

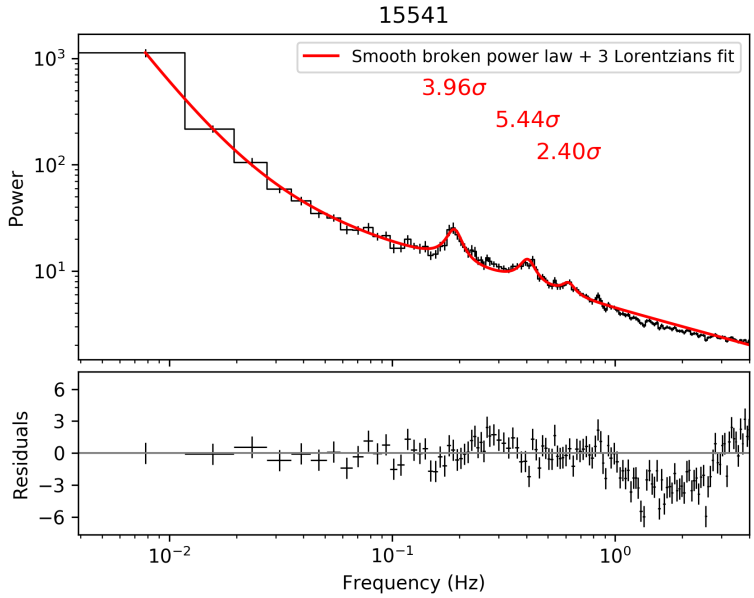

Figure 4.13: Power spectrum and QPO structures in MJD 55541 observations.

et. al., 2010]. This analysis is conducted to cross-check the QPO significance using a slightly different continuum model, and to check if our QPO analysis yields similar results consistent with the reported values. Thus, using the same procedure described above, all the time windows in the mentioned time intervals are averaged to create a single frame. The resulting power spectrum is fitted by our Python code. The power

spectrum and the fit is shown at Figure 4.13 and the parameters of the QPO of both analyses are given at Table 4.3. Our analysis returns similar results to the previously reported values of the QPO [37]. As the parameters to create the power spectrum and the fitting details are not given by [37], slightly different results of QPO significance possibly arises due to using different continuum models in power spectrum fitting.

CHAPTER 5

SUMMARY AND CONCLUSION

In this thesis, Swift and RXTE observations of MAXI J1409-619 are analyzed in detail. MAXI J1409-619 is an accretion-powered, Be type high mass X-ray binary system candidate. It was first detected in October 2010, and observed by both instruments until February 2011. Except for a couple ATels briefly describing its properties, and a few articles mentioning it, no in-depth analysis of MAXI J1409-619 has been published before. 15 observations of Swift (19.2 ks) and 50 observations of RXTE (135 ks) take place in the scope of the analysis.

The time-resolved spectra of RXTE and Swift confirm the previous findings of the ATels. A power law and iron line emission at 6.4 keV, modified with photoelectric absorption give the best fits for the obtained spectra. Besides, power law component has a high energy exponential cutoff during the outburst stage, and the cutoff frequency apparently decreases as the outburst progresses. Absence of a meaningful cutoff value before and after the outburst might be attributed to the insufficient sensitivity of the instruments. One-time nature and the relatively long duration of the outburst ($\sim$2 months) suggest that the binary system exhibited a type II outburst. No detection of the source at the quiescent stage before, which means that the flux at outburst rose some orders of magnitude, supports this assertion. The peak flux of the source (corrected for absorption) is calculated to be 1.96×10^{-9} erg s^{-1} cm^{-2}. Assuming a distance of $\sim$14.5 kiloparsecs [40], the peak luminosity of the system is predicted to be $L_{X\text{-}ray} \sim 4.9\times10^{37}$ erg s^{-1}, reaching in early December 2010. The discovery of an optical Be star companion would concretize the BeXB classification of the system.

At the onset of the outburst stage, periodicity of $\sim$503 seconds in the light curves is observed, further confirming that the source is an accretion-powered X-ray pulsar.

Phase-resolved spectroscopy analysis in selected RXTE data indicates that the pulse profile is double peaked. Each peak corresponds to the emission from the hotspots at the magnetic poles of the pulsar. The X-ray emission is harder during the pulse maxima, implying that the emission is harder at the hot spots. The Gaussian iron line is observed to be broadened at the pulse minimas, which might be attributed to the increased visibility of 7.04 keV Kβ line due to decreased interference of the hot spot emission, alongside 6.4 keV Kα line emission.

Finally, QPO analysis of MAXI J1409-619 is done by fitting the power spectra with a smooth broken power law model in addition to Lorentzian components for QPO excess peaks. The analysis of the data gathered on MJD 55541 revealed a QPO with two harmonics at (0.190$\pm$0.001) Hz, (0.405$\pm$0.021) Hz, and (0.618$\pm$0.080) Hz; and with statistical significances of 3.96σ, 5.44σ and 2.40σ respectively. These results are consistent with the previous reporting. Besides, the existence of the QPOs verify the existence of an accretion disk during the observation period, and the milliHertz range of the QPOs supports that the source is a HMXB pulsar. Furthermore, time-resolved QPO analysis demonstrates that QPOs exist only at the outburst stage of the source, and in a fluctuating manner. QPO components do not always appear in the power spectra, and the detected QPOs have varying amplitudes over time. Though not statistically significant in many cases, QPO harmonics are occasionally observed as well. Another interesting result is that the QPO frequency is consistently shifted from $\sim$0.2 Hz to $\sim$0.1 Hz as the outburst progresses, meaning that QPOs are slowed down with decreasing flux. Therefore, corresponding QPO production region radius increases from $\sim 5\times10^8$ cm to $\sim 8\times10^8$ cm as the outburst fades. Using the equations 1.1, 1.2, 1.6 and 1.7, the magnetic field of the source is calculated as

$$B \approx 2^{\frac{1}{4}}\ 0.52^{-\frac{7}{4}}(2\pi\nu_K)^{-\frac{7}{6}}(GM)^{\frac{1}{3}}L^{\frac{1}{2}}R^{-\frac{5}{2}} \tag{5.1}$$

which is in the order of 1×10^{13} Gauss.

REFERENCES

[1] M. Orellana and G. E. Romero, "Gamma-Ray Emission from Be/X-ray Binaries," *Astrophysics and Space Science*, vol. 297, pp. 167–178, 2005.

[2] M. Matsuoka, K. Kawasaki, S. Ueno, H. Tomida, M. Kohama, M. Suzuki, Y. Adachi, M. Ishikawa, T. Mihara, M. Sugizaki, N. Isobe, Y. Nakagawa, H. Tsunemi, E. Miyata, N. Kawai, J. Kataoka, M. Morii, A. Yoshida, H. Negoro, M. Nakajima, Y. Ueda, H. Chujo, K. Yamaoka, O. Yamazaki, S. Nakahira, T. You, R. Ishiwata, S. Miyoshi, S. Eguchi, K. Hiroi, H. Katayama, and K. Ebisawa, "The MAXI Mission on the ISS: Science and Instruments for Monitoring All Sky X-Ray Images," *Publications of the Astronomical Society of Japan*, vol. 61, no. 5, pp. 999–1010, 2009.

[3] W. Baade and F. Zwicky, "Remarks on Super-Novae and Cosmic Rays," *Physical Review*, vol. 46, pp. 76–77, 1934.

[4] R. Giacconi, H. Gursky, F. R. Paolini, and B. B. Rossi, "Evidence for x Rays From Sources Outside the Solar System," *Physical Review Letters*, vol. 9, pp. 439–443, 1962.

[5] I. S. Shklovsky, "On the Nature of the Source of X-Ray Emission of Sco XR-1.," *The Astrophysical Journal*, vol. 148, pp. L1–L4, 1967.

[6] A. Hewish, S. J. Bell, J. D. H. Pilkington, P. F. Scott, and R. A. Collins, "Observation of a Rapidly Pulsating Radio Source," *Nature*, vol. 217, pp. 709–713, 1968.

[7] P. Ghosh, *Rotation and Accretion Powered Pulsars*. World Scientific, 2007.

[8] F. K. Lamb, C. J. Pethick, and D. Pines, "A Model for Compact X-Ray Sources: Accretion by Rotating Magnetic Stars," *The Astrophysical Journal*, vol. 184, pp. 271–290, 1973.

[9] L. Bildsten, D. Chakrabarty, J. Chiu, M. H. Finger, D. T. Koh, R. W. Nelson, T. A. Prince, B. C. Rubin, D. M. Scott, M. Stollberg, B. A. Vaughan, C. A. Wilson, and R. B. Wilson, "Observations of Accreting Pulsars," *The Astrophysical Journal Supplement Series*, vol. 113, no. 2, pp. 367–408, 1997.

[10] R. H. D. Corbet, "The three types of high-mass X-ray pulsator," *Monthly Notices of the Royal Astronomical Society*, vol. 220, pp. 1047–1056, 1986.

[11] P. Reig, "Be/X-ray binaries," *Astrophysics and Space Science*, vol. 332, pp. 1–29, mar 2011.

[12] M. S. Longair, *High Energy Astrophysics, 3rd ed.* Cambridge University Press, 2011.

[13] R. H. D. Corbet, "Be/neutron star binaries : a relationship between orbital period and neutron star spin period.," *Astronomy and Astrophysics*, vol. 141, pp. 91–93, 1984.

[14] L. B. F. M. Waters and M. H. van Kerkwijk, "The relation between orbital and spin periods in massive X-ray binaries," *Astronomy and Astrophysics*, vol. 223, pp. 196–206, 1989.

[15] J. Casares, I. Negueruela, M. Ribó, I. Ribas, J. M. Paredes, A. Herrero, and S. Simón-Díaz, "A Be-type star with a black-hole companion," *Nature*, vol. 505, pp. 378–381, 2014.

[16] M. van der Klis, F. Jansen, J. van Paradijs, W. H. G. Lewin, E. P. J. van den Heuvel, J. E. Trumper, and M. Szatjno, "Intensity-dependent quasi-periodic oscillations in the X-ray flux of GX5-1," *Nature*, vol. 316, pp. 225–230, 1985.

[17] L. Angelini, L. Stella, and A. N. Parmar, "The Discovery of 0.2 HZ Quasi-periodic Oscillations in the X-Ray Flux of the Transient 42 Second Pulsar EXO 2030+375," *Astrophysical Journal*, vol. 346, p. 906, 1989.

[18] M. R. Dugair, G. K. Jaisawal, S. Naik, and S. N. A. Jaaffrey, "Detection of a Variable QPO at ˜41mHz in the Be/X-ray Transient Pulsar 4U 0115+634," *Monthly Notices of the Royal Astronomical Society*, vol. 434, no. 3, pp. 2458–2464, 2013.

[19] M. van der Klis, F. Jansen, J. van Paradijs, W. H. G. Lewin, M. Sztajno, and J. Truemper, "Correlation between Spectral State and Quasi-periodic Oscillation Parameters in GX 5-1," *Astrophysical Journal*, vol. 313, pp. L19–L23, 1987.

[20] A. Camero-Arranz, M. H. Finger, C. A. Wilson-Hodge, P. Jenke, I. Steele, M. J. Coe, J. Gutierrez-Soto, P. Kretschmar, I. Caballero, J. Yan, J. Rodríguez, J. Suso, G. Case, M. L. Cherry, S. Guiriec, and V. A. McBride, "X-Ray and Optical Observations of A 0535+26," *Astrophysical Journal*, vol. 754, p. 20, 2012.

[21] P. Ghosh and F. K. Lamb, "Accretion by rotating magnetic neutron stars. III. Accretion torques and period changes in pulsating X-ray sources.," *The Astrophysical Journal*, vol. 234, pp. 296–316, 1979.

[22] M. A. Alpar and J. Shaham, "Is GX5 - 1 a millisecond pulsar?," *Nature*, vol. 316, pp. 239–241, 1985.

[23] F. K. Lamb, N. Shibazaki, M. A. Alpar, and J. Shaham, "Quasi-periodic oscillations in bright galactic-bulge X-ray sources," *Nature*, vol. 317, pp. 681–687, 1985.

[24] Swift Science Center, "The Swift Technical Handbook," 2017.

[25] D. N. Burrows, J. E. Hill, J. A. Nousek, J. A. Kennea, A. Wells, J. P. Osborne, A. F. Abbey, A. Beardmore, K. Mukerjee, A. D. T. Short, G. Chincarini, S. Campana, O. Citterio, A. Moretti, C. Pagani, G. Tagliaferri, P. Giommi, M. Capalbi, F. Tamburelli, L. Angelini, G. Cusumano, H. W. Bräuninger, W. Burkert, and G. D. Hartner, "The Swift X-Ray Telescope," *Space Science Reviews*, vol. 120, no. 3-4, pp. 165–195, 2005.

[26] "Appendix F: The XTE Technical Appendix," 2006.

[27] K. Jahoda, C. B. Markwardt, Y. Radeva, A. Rots, M. J. Stark, J. H. Swank, T. E. Strohmayer, and W. Zhang, "Calibration of the Rossi X-ray Timing Explorer Proportional Counter Array," *The Astrophysical Journal Supplement Series*, vol. 163, no. 2, pp. 401–423, 2006.

[28] H. Negoro and M. team, "Discovery of 17 X-ray Transients with MAXI/GSC and their Nature," in *7 years of MAXI: monitoring X-ray Transients, held 5-7*

December 2016 at RIKEN (M. Serino, M. Shidatsu, W. Iwakiri, and T. Mihara, eds.), (Tokyo, Japan), p. 15, 2017.

[29] T. Mihara, M. Nakajima, M. Sugizaki, M. Serino, M. Matsuoka, M. Kohama, K. Kawasaki, H. Tomida, S. Ueno, N. Kawai, J. Kataoka, M. Morii, A. Yoshida, K. Yamaoka, S. Nakahira, H. Negoro, N. Isobe, M. Yamauchi, and I. Sakurai, "Gas Slit Camera (GSC) onboard MAXI on ISS," *Publications of the Astronomical Society of Japan*, vol. 63, no. sp3, pp. S623–S634, 2011.

[30] M. Sugizaki, T. Mihara, M. Serino, T. Yamamoto, M. Matsuoka, M. Kohama, H. Tomida, S. Ueno, N. Kawai, M. Morii, K. Sugimori, S. Nakahira, K. Yamaoka, A. Yoshida, M. Nakajima, H. Negoro, S. Eguchi, N. Isobe, Y. Ueda, and H. Tsunemi, "In-Orbit Performance of MAXI Gas Slit Camera (GSC) on ISS," *Publications of the Astronomical Society of Japan*, vol. 63, no. sp3, pp. S635–S644, 2011.

[31] K. Yamaoka, S. Nakahira, H. Negoro, N. Kawai, A. Uzawa, K. Yamazaki, T. Matsumura, Y. Tsuboi, K. Kawasaki, S. Ueno, H. Tomida, M. Kohama, M. Ishikawa, T. Mihara, M. Sugizaki, M. Serino, Y. E. Nakagawa, T. Yamamoto, T. Sootome, M. Matsuoka, M. Morii, K. Sugimori, R. Usui, A. Yoshida, H. Tsunemi, M. Kimura, M. Nakajima, H. Ozawa, F. Suwa, Y. Ueda, N. Isobe, S. Eguchi, K. Hiroi, A. Daikyuji, and Maxi Team, "MAXI/GSC detects an X-ray transient MAXI J1409-619," *The Astronomer's Telegram*, vol. 2959, p. 1, Oct. 2010.

[32] J. A. Kennea, H. Krimm, P. Romano, V. Mangano, P. Curran, and P. Evans, "MAXI J1409-619: Swift localization and identification as a new X- ray transient," *The Astronomer's Telegram*, vol. 2962, p. 1, Oct. 2010.

[33] K. Yamaoka, P. Kaaret, S. Nakahira, I. Takakashi, A. Yoshida, M. Morii, N. Kawai, H. Negoro, M. Nakajima, Y. Ueda, M. Suzuki, and T. Yamamoto, "RXTE follow-up observations of MAXI J1409-619," *The Astronomer's Telegram*, vol. 2969, p. 1, Oct. 2010.

[34] J. A. Kennea, P. Curran, H. Krimm, P. Romano, V. Mangano, P. A. Evans, K. Yamaoka, and D. N. Burrows, "Swift detection of an ~500s period in MAXI J1409-619," *The Astronomer's Telegram*, vol. 3060, p. 1, Dec. 2010.

[35] S. Ueno, M. Sugizaki, H. Negoro, N. Kawai, H. Tomida, M. Kohama, M. Ishikawa, T. Mihara, Y. E. Nakagawa, M. Serino, T. Yamamoto, T. Sootome, M. Matsuoka, M. Morii, K. Sugimori, R. Usui, A. Yoshida, K. Yamaoka, S. Nakahira, H. Tsunemi, M. Kimura, H. Kitayama, M. Nakajima, H. Ozawa, F. Suwa, Y. Ueda, N. Isobe, S. Eguchi, K. Hiroi, M. Shidatsu, A. Daikyuji, Y. Tsuboi, A. Uzawa, T. Matsumura, and K. Yamazaki, "MAXI/GSC detects X-ray re-brightening of MAXI J1409-619," *The Astronomer's Telegram*, vol. 3067, p. 1, Dec. 2010.

[36] A. Camero-Arranz, M. H. Finger, and P. Jenke, "Fermi/GBM detects pulsations of the transient source MAXI J1409-619," *The Astronomer's Telegram*, vol. 3069, p. 1, Dec. 2010.

[37] R. Kaur, P. Casella, M. Linares, D. Altamirano, A. Patruno, M. Armas-Padilla, Y. Cavecchi, N. Degenaar, D. Russell, M. Kalamkar, M. van der Klis, A. Watts, R. Wijnands, and N. Rea, "Discovery of 0.19 Hz QPO in MAXI J1409-619," *The Astronomer's Telegram*, vol. 3082, p. 1, Dec. 2010.

[38] J. Devasia, M. James, B. Paul, and K. Indulekha, "Timing and spectral studies of the transient X-ray pulsar GX 304-1 during an outburst," *Monthly Notices of the Royal Astronomical Society*, vol. 417, pp. 348–358, Oct 2011.

[39] V. Sguera, M. Orlandini, F. Frontera, A. Bazzano, and A. J. Bird, "Archival BeppoSAX/MECS observation of MAXI J1409-619 and INTEGRAL upper limit," *The Astronomer's Telegram*, vol. 2965, p. 1, Oct. 2010.

[40] M. Orlandini, F. Frontera, N. Masetti, V. Sguera, and L. Sidoli, "BeppoSAX Observations of the X-Ray Pulsar MAXI J1409-619 in Low State: Discovery of Cyclotron Resonance Features," *Astrophysical Journal*, vol. 748, p. 86, Apr 2012.

[41] W. Coburn, W. A. Heindl, R. E. Rothschild, D. E. Gruber, I. Kreykenbohm, J. Wilms, P. Kretschmar, and R. Staubert, "Magnetic Fields of Accreting X-Ray Pulsars with the ROSSI X-Ray Timing Explorer," *The Astrophysical Journal*, vol. 580, pp. 394–412, Nov. 2002.

[42] M. M. Serim, e. Şahiner, D. Çerri-Serim, S. Ç. İnam, and A. Baykal,

"Comprehensive timing and X-ray spectral analysis of GX 1+4," *Monthly Notices of the Royal Astronomical Society*, vol. 469, pp. 2509–2516, 2017.

[43] "SmoothlyBrokenPowerLaw1D — Astropy v3.1.1." http://docs.astropy.org/en/stable/api/astropy.modeling.powerlaws.SmoothlyBrokenPowerLaw1D.html, Accessed: 01 Jan 2019.

[44] "MOdel." https://wwwastro.msfc.nasa.gov/qdp/help/model.html, Accessed: 1 Jan 2019.

[45] "F-test — PyAstronomy 0.13.0 documentation." https://www.hs.uni-hamburg.de/DE/Ins/Per/Czesla/PyA/PyA/pyaslDoc/aslDoc/statTest.html, Accessed: 1 Jan 2019.

Appendix A

RXTE PCA OBSERVATION LIST

Table A.1: List of RXTE PCA observations.

ObsID	Date	Date (MJD)	Exposure (s)
95358-02-01-02	2010-10-22	55491	1169
95358-02-01-00	2010-10-22	55491	5037
95358-02-01-01	2010-10-23	55492	1521
95358-02-01-03	2010-10-24	55493	1337
95358-02-02-02	2010-10-26	55495	934
95358-02-02-01	2010-10-27	55496	920
95358-02-02-00	2010-10-28	55497	10414
95358-02-03-00	2010-10-29	55498	858
95358-02-03-01	2010-10-30	55499	935
95358-02-03-02	2010-10-31	55500	1343
95358-02-03-03	2010-11-01	55501	835
95358-02-03-04	2010-11-02	55502	1141
95358-02-03-05	2010-11-03	55503	663
95358-02-03-06	2010-11-04	55504	925
95358-02-04-00	2010-12-04	55534	8338
95358-02-04-01	2010-12-04	55534	1424
95441-01-01-01	2010-12-10	55540	981
95441-01-01-02	2010-12-11	55541	5163
95441-01-01-00	2010-12-11	55541	13836
95441-01-01-03	2010-12-12	55542	15018
95441-01-01-04	2010-12-13	55543	3589
95441-01-01-05	2010-12-14	55544	3531
95441-01-01-06	2010-12-15	55545	3926
95441-01-01-07	2010-12-16	55546	3589
95441-01-02-00	2010-12-17	55547	4310
95441-01-02-01	2010-12-18	55548	1946
95441-01-02-03	2010-12-19	55549	1767
95441-01-02-04	2010-12-20	55550	3175

Continued on next page

Table A.1 – Continued from previous page

ObsID	Date	Date (MJD)	Exposure (s)
95441-01-02-05	2010-12-21	55551	1199
95441-01-02-02	2010-12-22	55552	802
95441-01-02-06	2010-12-22	55552	802
95441-01-02-07	2010-12-23	55553	1075
95441-01-03-00	2010-12-24	55554	1768
95441-01-03-01	2010-12-25	55555	1289
95441-01-03-02	2010-12-26	55556	2011
95441-01-03-03	2010-12-28	55558	1277
95441-01-03-04	2010-12-29	55559	1710
95441-01-03-05	2010-12-30	55560	1624
96410-01-01-00	2011-01-05	55566	3541
96410-01-02-00	2011-01-10	55571	2380
96410-01-02-01	2011-01-12	55573	2874
96410-01-03-00	2011-01-15	55576	2713
96410-01-03-02	2011-01-16	55577	1412
96410-01-03-01	2011-01-19	55580	2250
96410-01-04-03	2011-01-22	55583	1197
96410-01-04-02	2011-01-22	55583	1198
96410-01-04-00	2011-01-22	55583	2363
96410-01-04-01	2011-01-26	55587	784
96410-01-05-00	2011-01-29	55590	838
96410-01-06-00	2011-02-05	55597	1313

Appendix B

TIME-RESOLVED ENERGY SPECTRA OF SWIFT XRT OBSERVATIONS

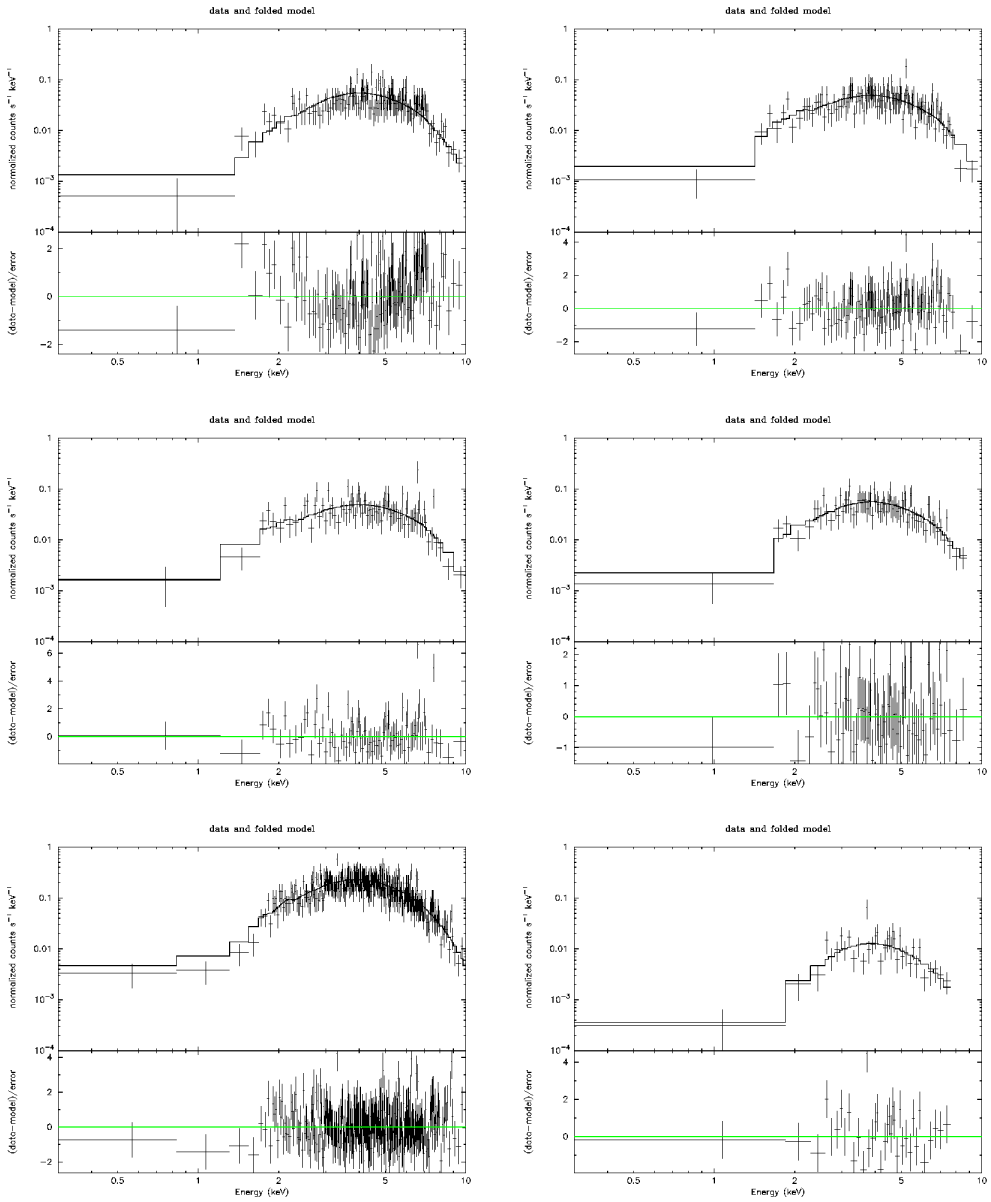

Figure B.1: The energy spectra of Swift XRT observations.

Appendix C

TIME-RESOLVED ENERGY SPECTRA OF RXTE PCA OBSERVATIONS

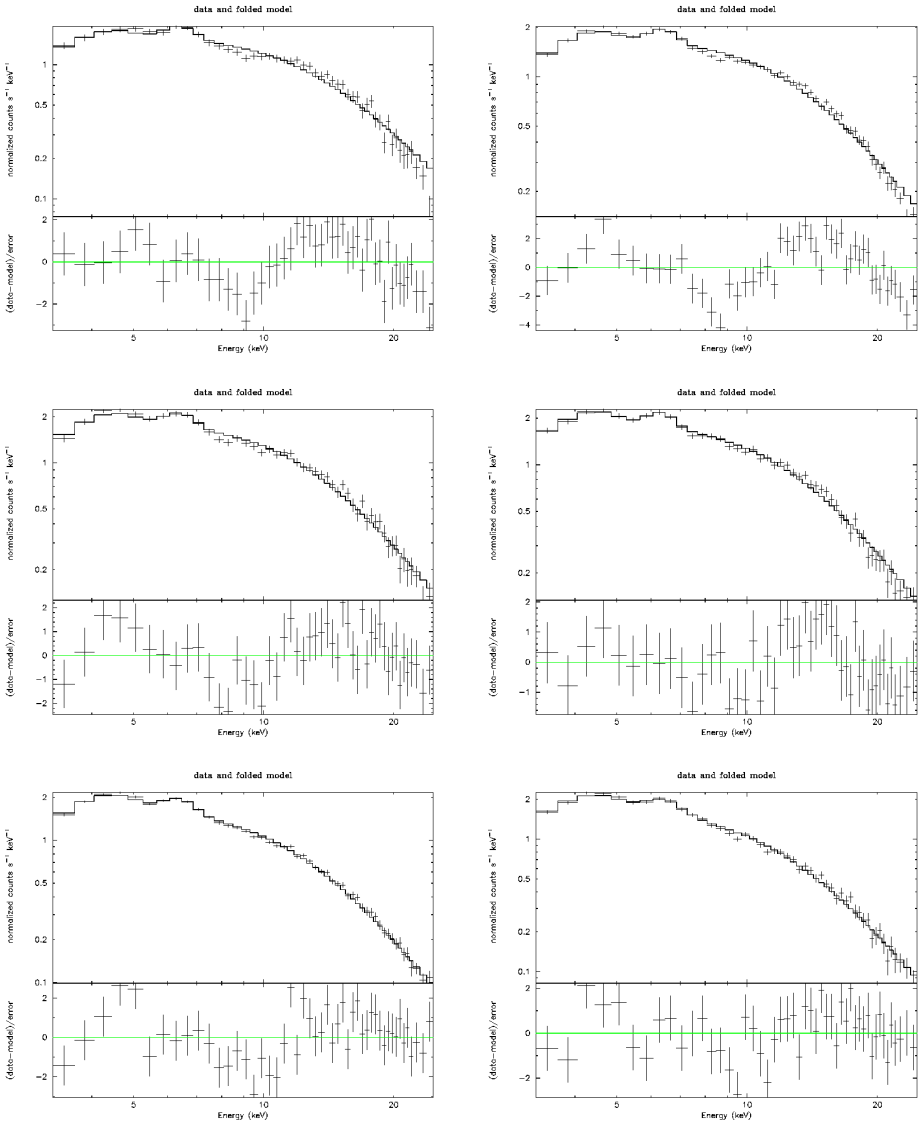

Figure C.1: The energy spectra of RXTE PCA observations in 95358 set.

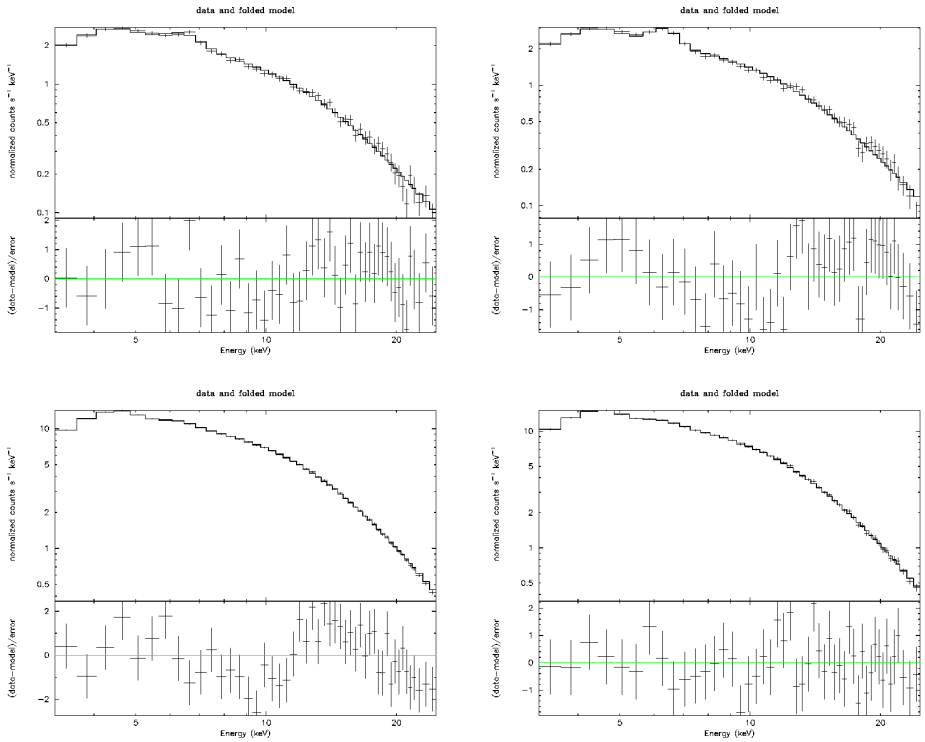

Figure C.2: The energy spectra of RXTE PCA observations in 95358 set. (continued)

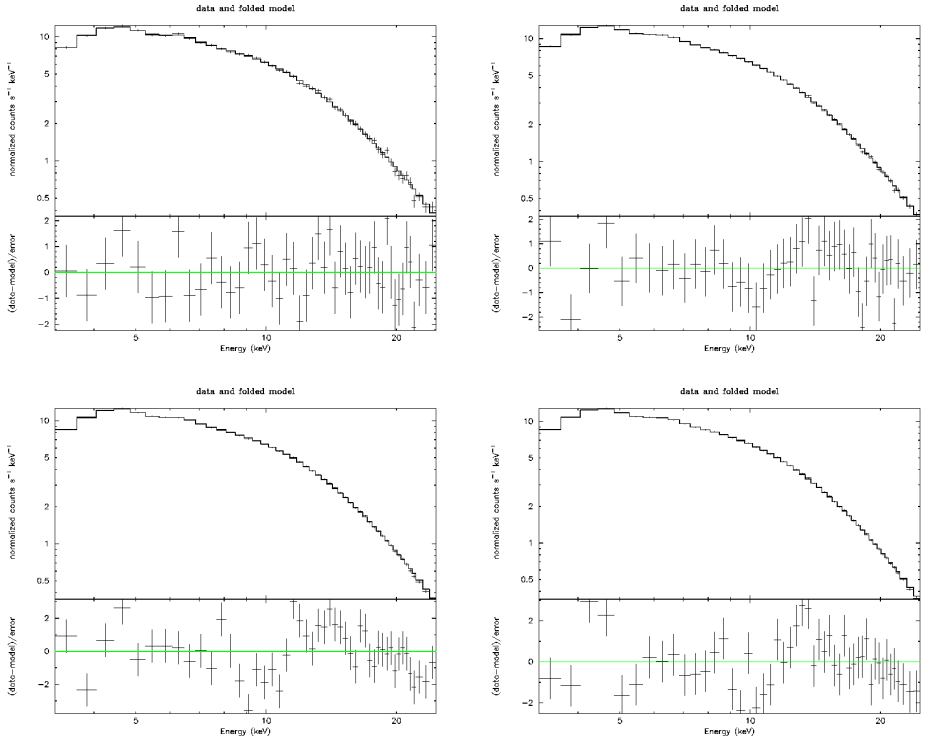

Figure C.3: The energy spectra of RXTE PCA observations in 95441 set.

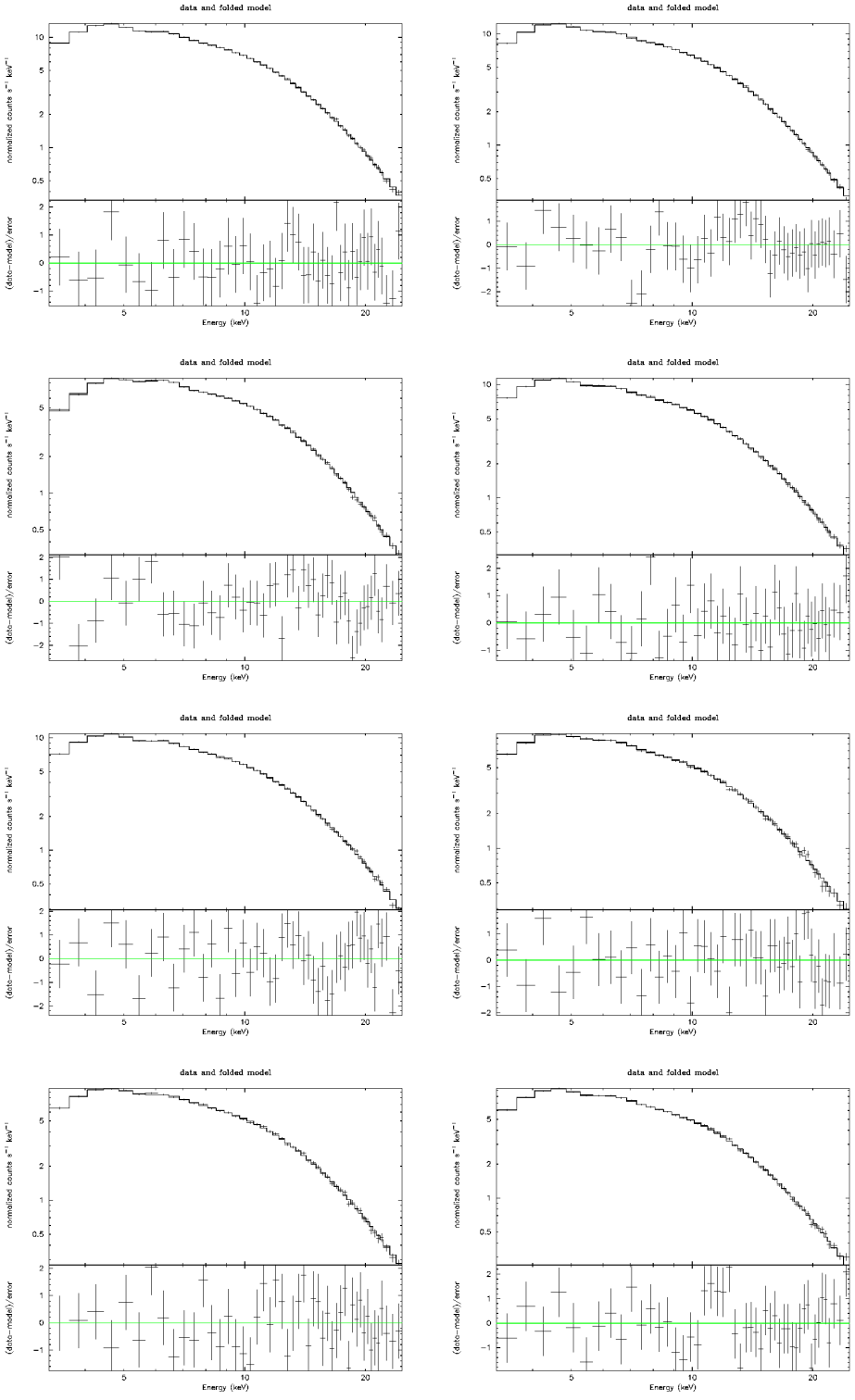

Figure C.4: The energy spectra of RXTE PCA observations in 95441 set. (continued)

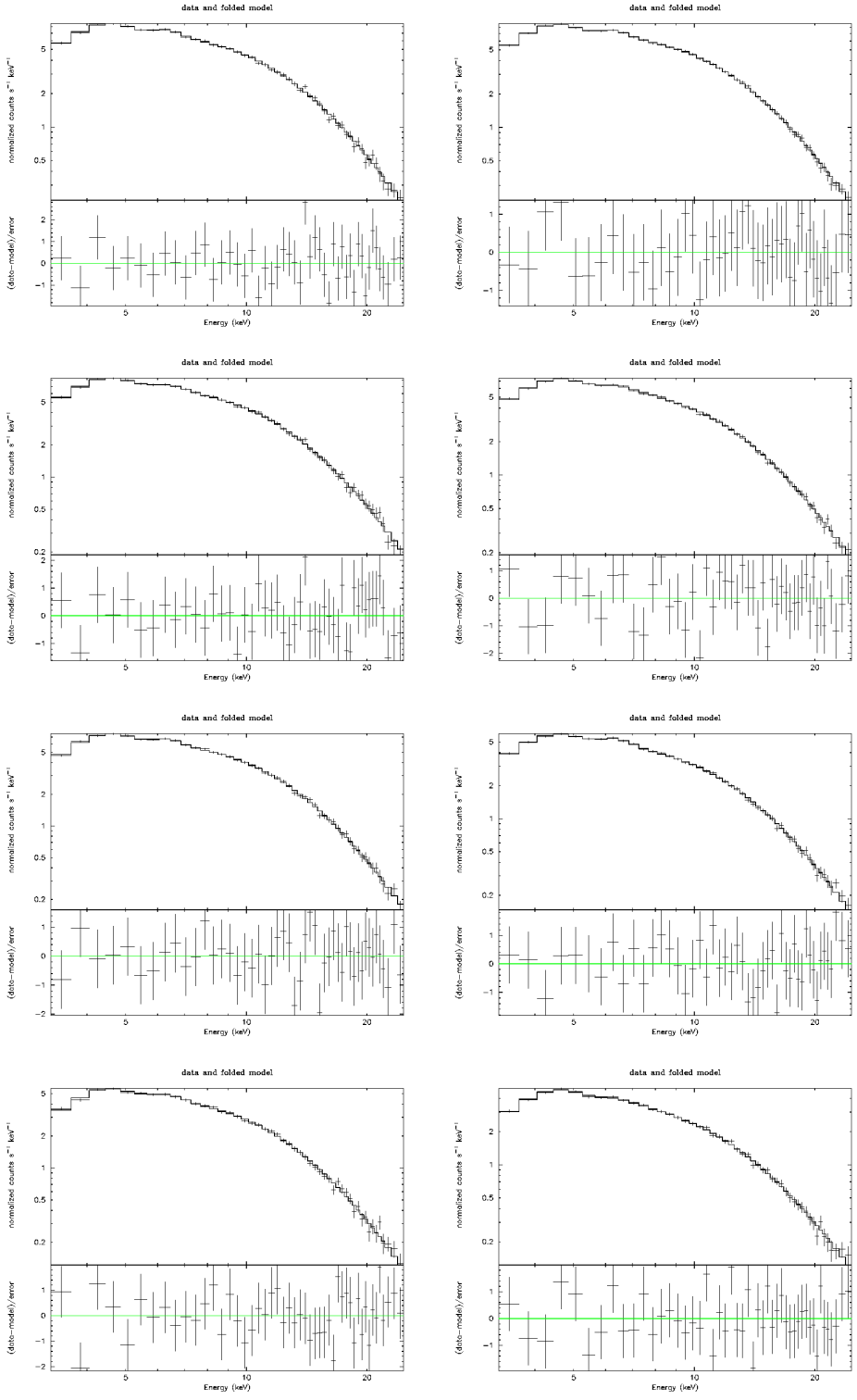

Figure C.5: The energy spectra of RXTE PCA observations in 95441 set. (continued)

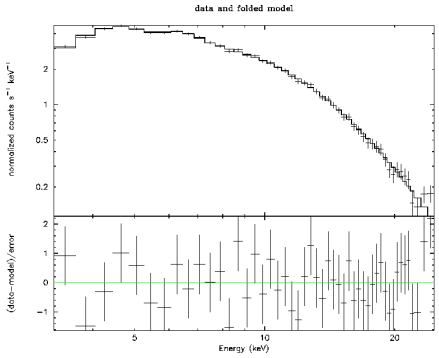

Figure C.6: The energy spectra of RXTE PCA observations in 95441 set. (continued)

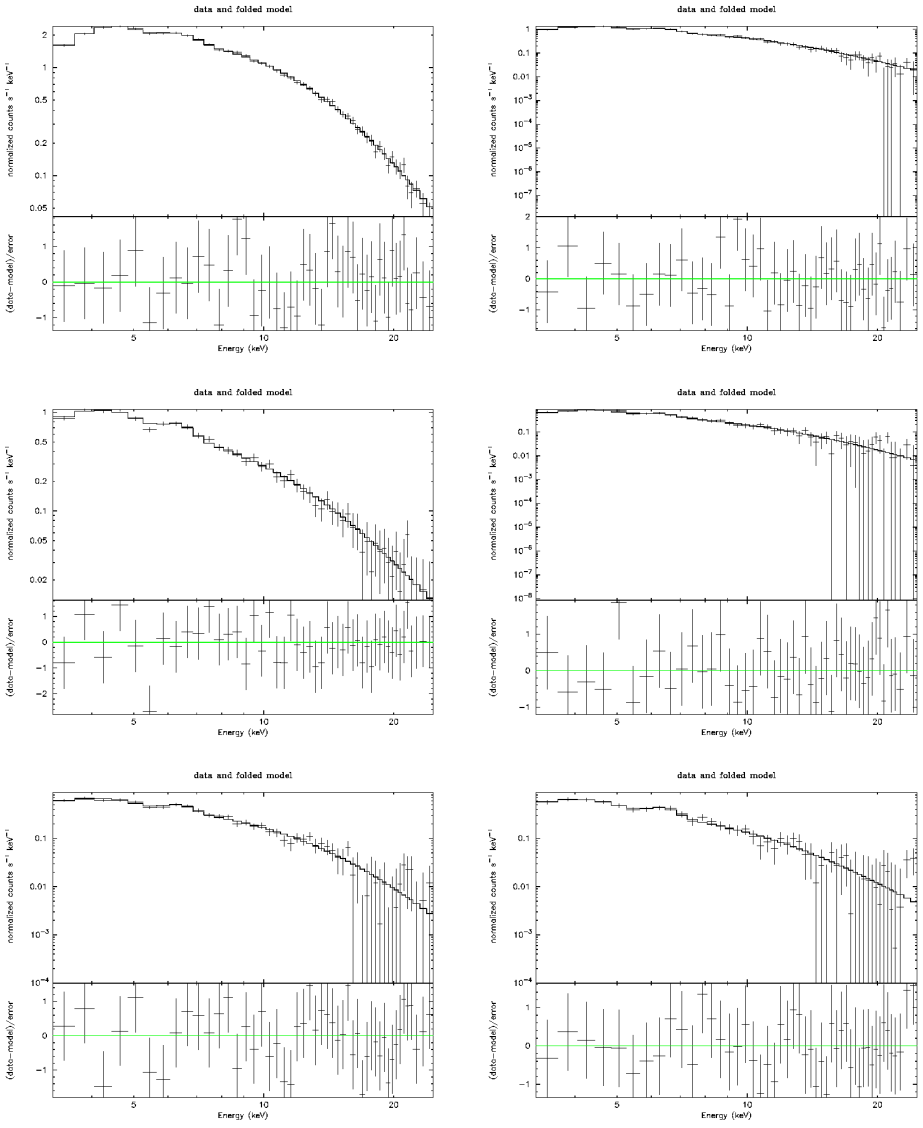

Figure C.7: The energy spectra of RXTE PCA observations in 96410 set.

Appendix D

POWER SPECTRA AND QPO PLOTS OF RXTE PCA OBSERVATIONS

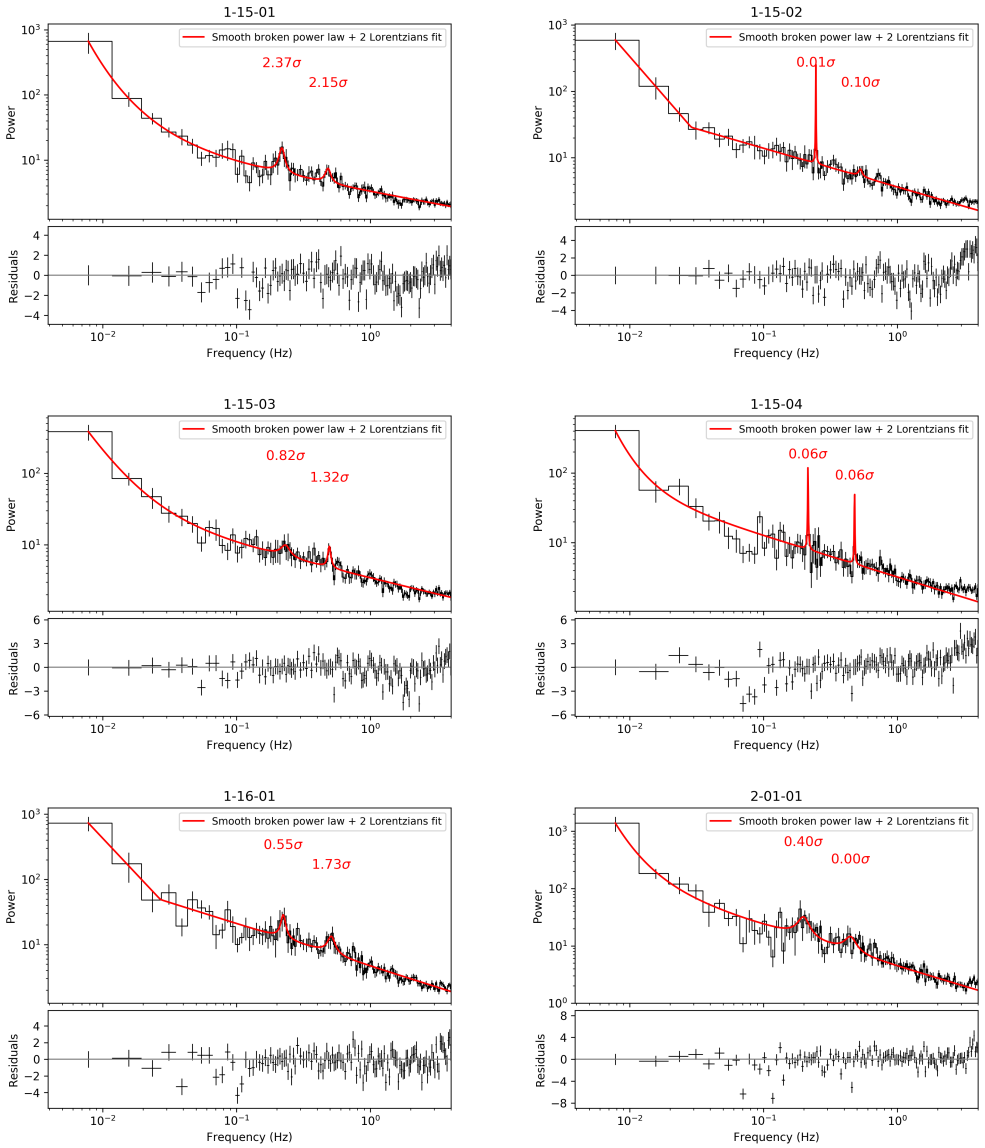

Figure D.1: Power spectra and QPO structures of RXTE PCA observations.

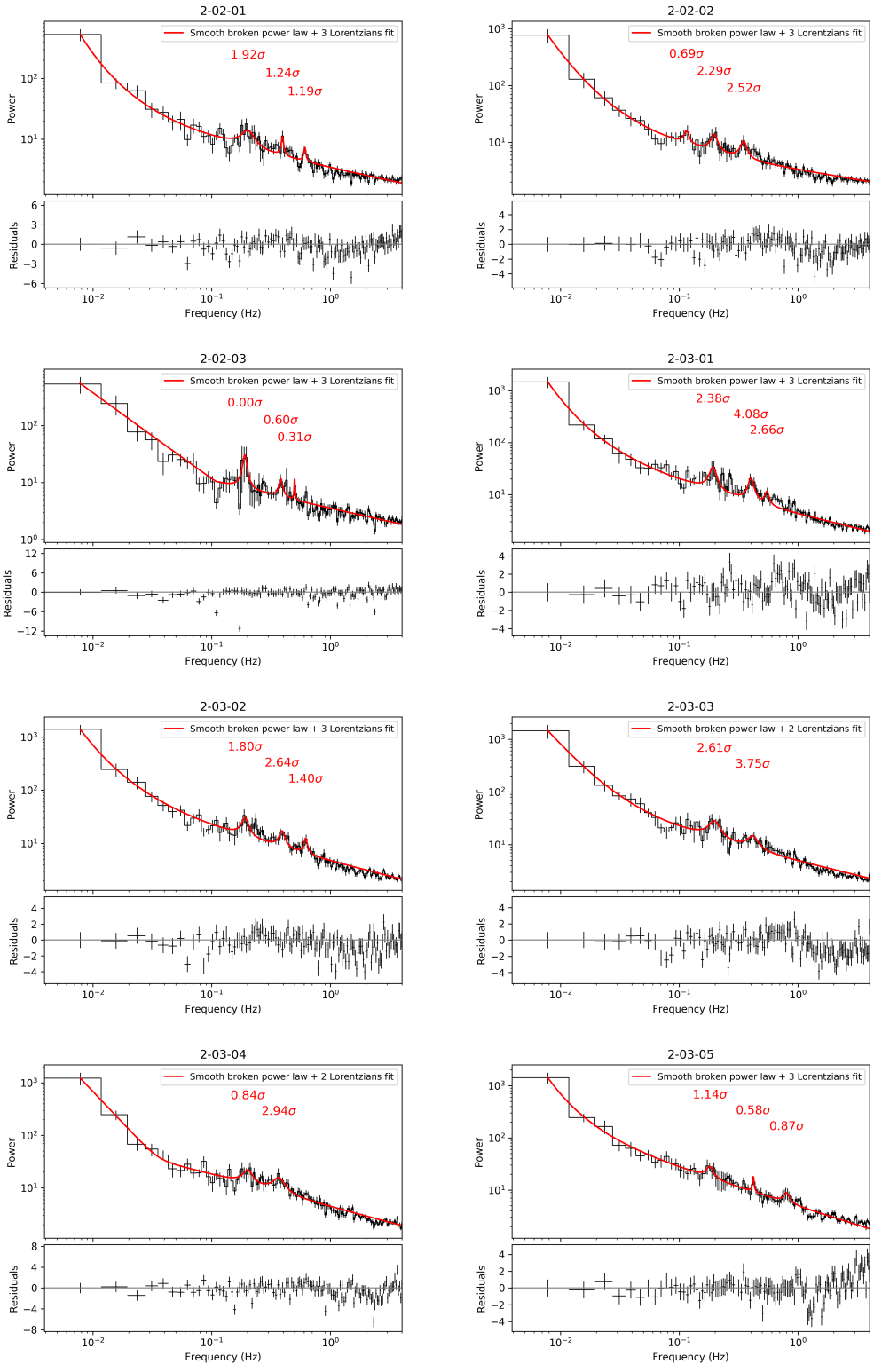

Figure D.2: Power spectra and QPO structures of RXTE PCA observations. (continued)

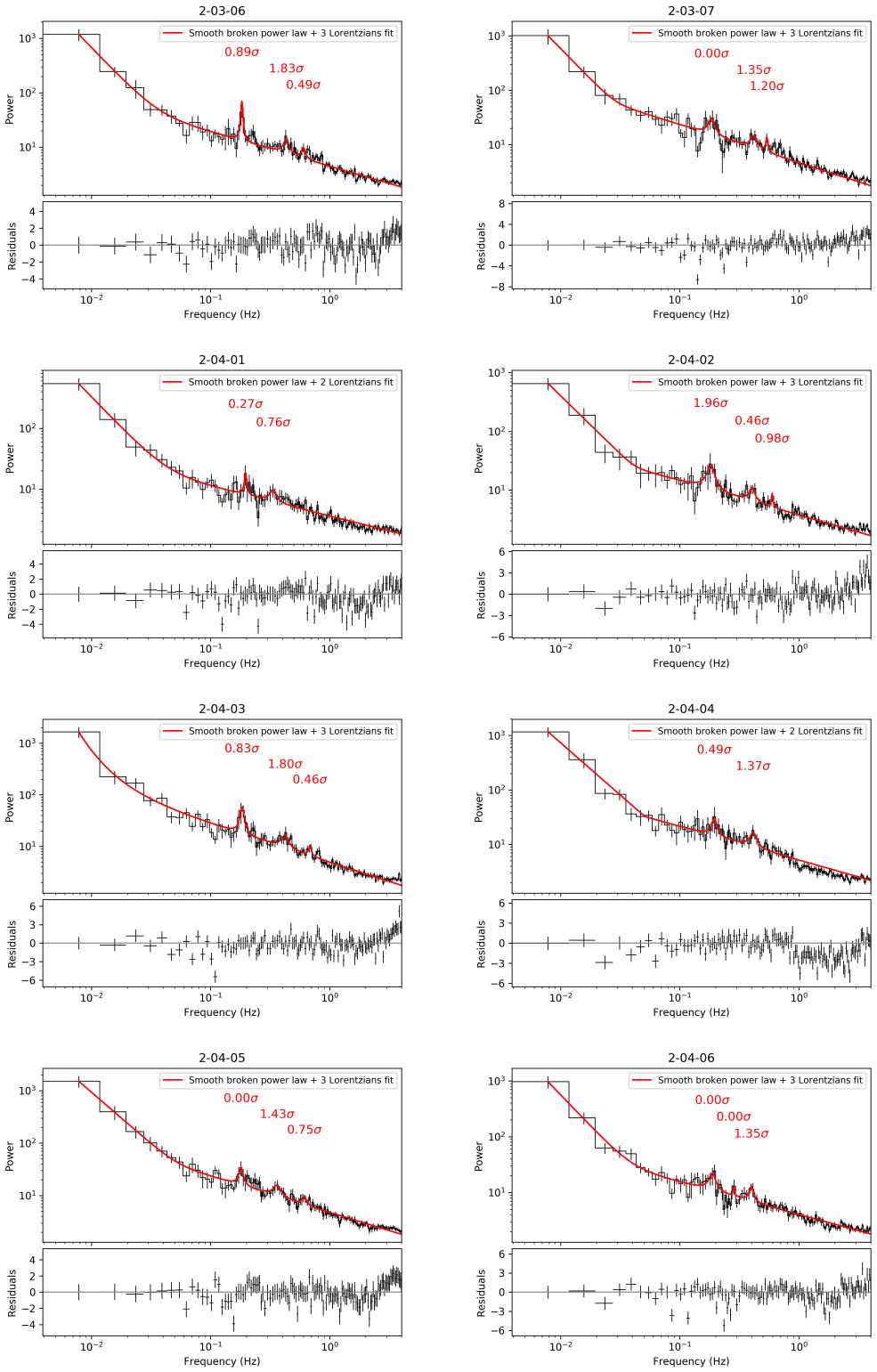

Figure D.3: Power spectra and QPO structures of RXTE PCA observations. (continued)

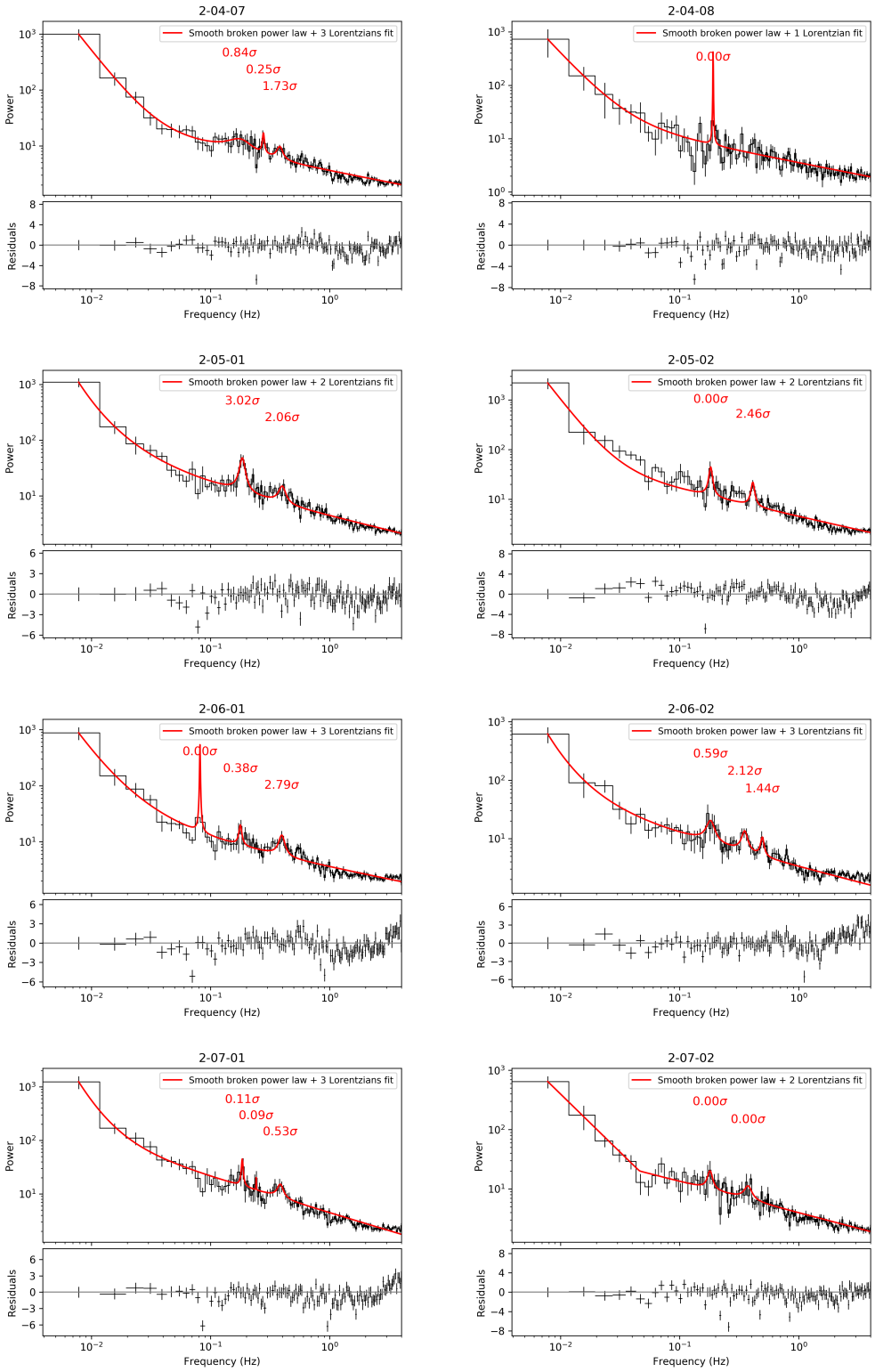

Figure D.4: Power spectra and QPO structures of RXTE PCA observations. (continued)

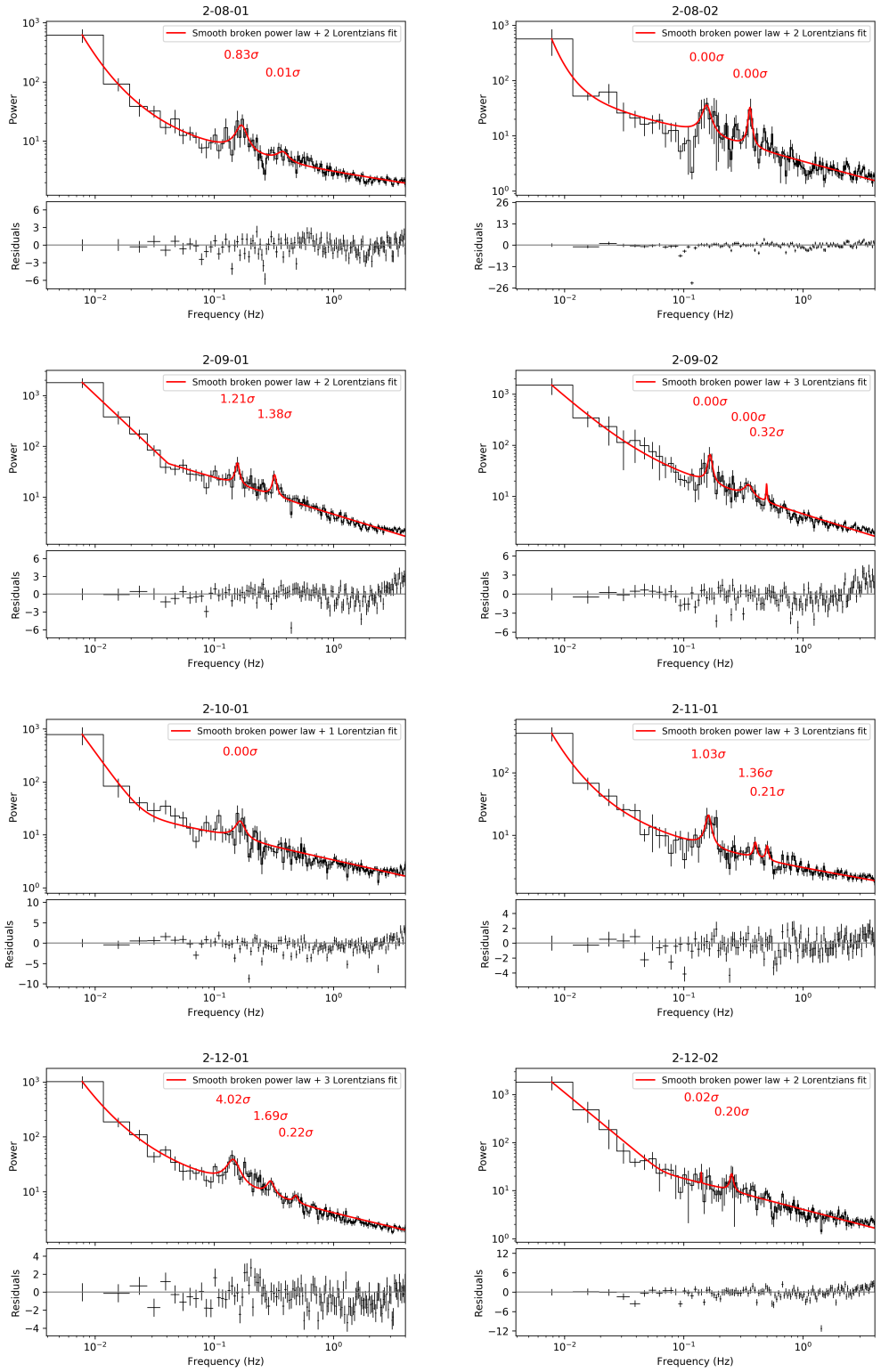

Figure D.5: Power spectra and QPO structures of RXTE PCA observations. (continued)

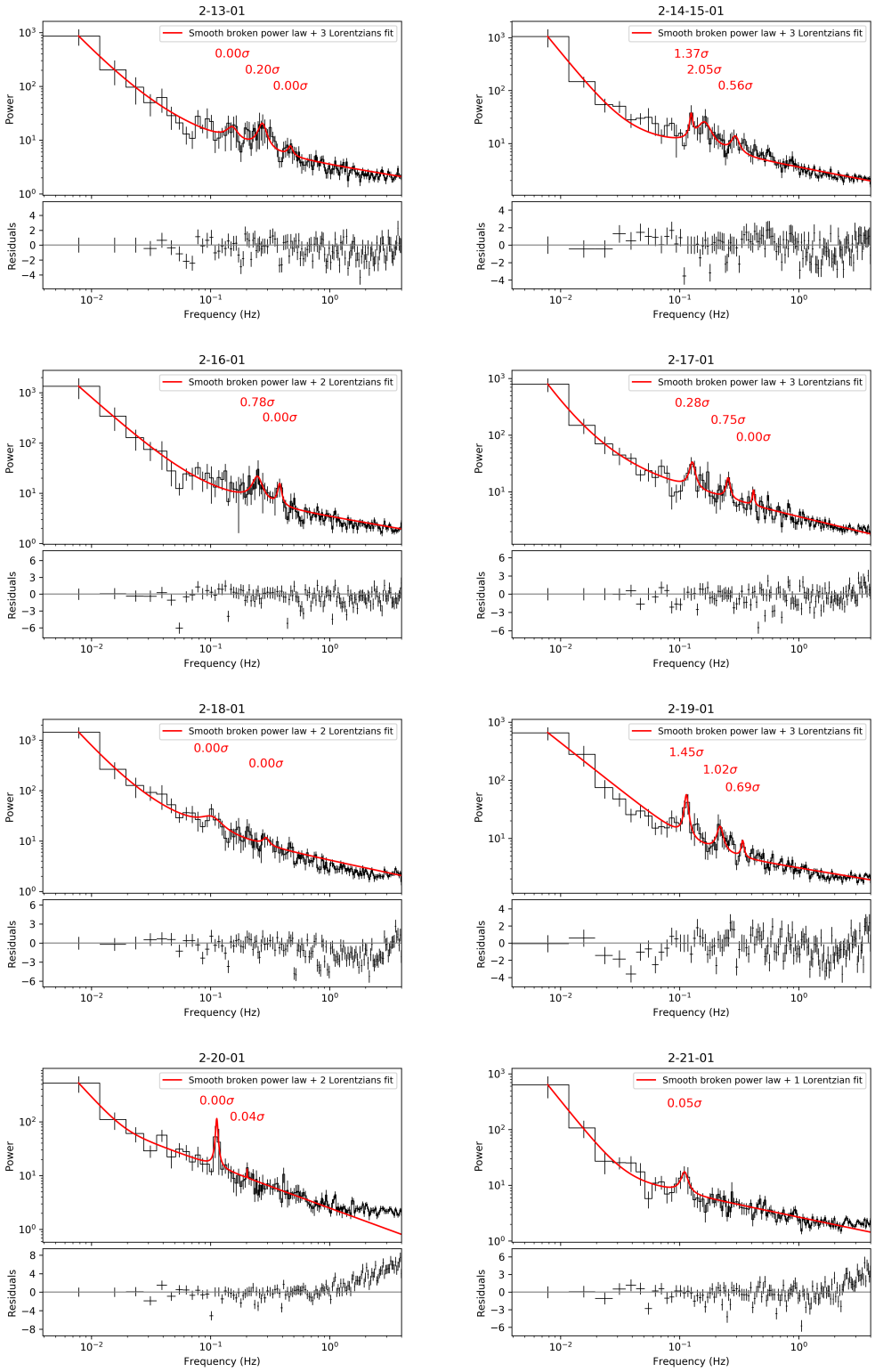

Figure D.6: Power spectra and QPO structures of RXTE PCA observations. (continued)

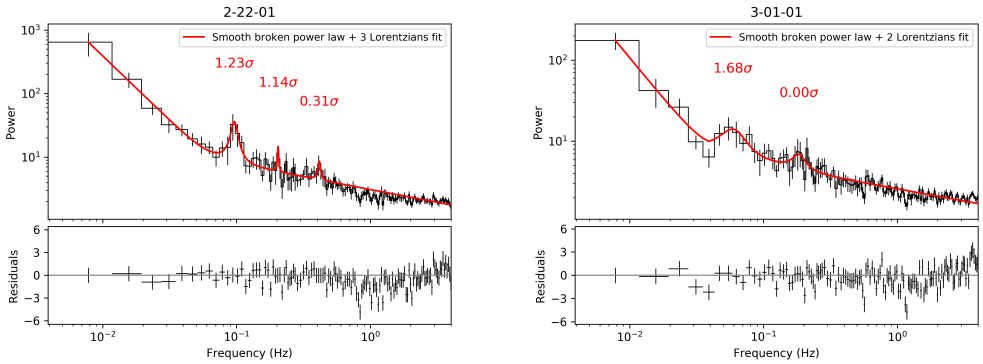

Figure D.7: Power spectra and QPO structures of RXTE PCA observations. (continued)